THESIS FOR THE DEGREE OF DOCTOR OF PHILOSOPHY

Productivity of Ferrous Alloys Produced by Powder Bed Fusion – Laser Beam

RASMUS GUNNEREK

Department of Industrial and Materials Science

CHALMERS UNIVERSITY OF TECHNOLOGY

Gothenburg, Sweden 2025

Productivity of Ferrous Alloys Produced by Powder Bed Fusion – Laser Beam

RASMUS GUNNEREK

ISBN 978-91-8103-228-4

Doktorsavhandlingar vid Chalmerska tekniska högskola

Ny serie nr 5686

ISSN 0346-718X

Department of Industrial and Materials Science

Chalmers University of Technology

SE-412 96 Gothenburg

Sweden

Telephone + 46 (0)31-772 1000

Chalmers digitaltryck

Gothenburg, Sweden 2025

Productivity of Ferrous Alloys Produced by Powder Bed Fusion – Laser Beam

RASMUS GUNNEREK

Department of Industrial and Materials Science

Chalmers University of Technology

Abstract

The thesis investigates the impact of increasing build rates on microstructure and properties, as-built surfaces and following post-AM processing in powder bed fusion – laser beam (PBF-LB) of 316L stainless steel and low-alloy steels (4130 and 4140).

The research demonstrates that increased build rates are possible when coupled with process control and appropriate post-processing. For 316L stainless steel, the study revealed that pore characteristics (distribution and orientation) can be tailored by adjusting layer thickness, scan speed and hatch distance. Extending this to low-alloy steels, optimized processing maps enabled high-density, crack-free parts at elevated build rates by managing defect formation and in-situ tempering.

To address the rough surfaces inherent to as-built components, both the electrochemical process Hirtisation® and chemical mechanical polishing (CMP) were investigated. Hirtisation® effectively reduced surface roughness through the removal of sintered powder and preferential attacks on melt pool boundaries. This microstructure-driven removal resulted in anisotropic surface patterns when the as-built surfaces exhibited anisotropy. The combination of chemical and mechanical material removal in CMP showed no influence on the developed microstructure while significantly reducing surface roughness and inducing compressive residual stresses. The mechanical interaction with the surfaces also led to the rounding of sample edges. Both surface treatments studied highlighted the need for further optimization regarding the amount of material removal required to fully eliminate subsurface defects.

Finally, the thesis established a link between pore characteristics and fatigue life of PBF-LB 316L fabricated with high build rate. Specifically, pores generated through increased hatch distances resulted in less scatter in fatigue life compared to those generated by increased scan speeds. This reduced scatter was attributed to the more similar pore distributions and pore morphologies observed in the former case. Furthermore, the application of surface treatments (Hirtisation® and CMP) was shown to double fatigue life by effectively reducing surface defects and surface roughness.

This research concludes that significant increases in PBF-LB build rates are attainable for ferrous alloys without compromising part quality, if process parameters are carefully controlled to manage microstructure and porosity, and appropriate post-processing is implemented to optimize surface integrity and fatigue performance, thereby broadening the industrial applicability of PBF-LB.

Keywords: additive manufacturing, powder bed fusion – laser beam, 316L stainless steel, low alloy steel, porosity, build speed, build rate, productivity in AM, process optimization.

Preface

This doctoral thesis details research conducted at the Department of Industrial and Materials Science at Chalmers University of Technology between September 2020 and June 2025. The studies have been conducted within the frame of Centre for Additive Manufacturing – Metal (CAM^2), with support by the Swedish Governmental Agency of Innovation Systems (Vinnova). Professor Eduard Hryha served as the main supervisor, with Dr. Zhuoer Chen (2020 – 2022) and Professor Uta Klement (2023 - 2025) as co-supervisors, and Professor Lars Nyborg acting as examiner. This thesis is based on the six appended papers listed below.

List of appended papers

Paper I: **Impact of high-productivity process parameters in powder bed fusion – laser beam on microstructure of stainless steel 316L**

Rasmus Gunnerek, Zhouer Chen and Eduard Hryha

European Journal of Materials, 2023

DOI: 10.1080/26889277.2023.2292987

Paper II: **Correlation between high build speed process parameters and pore characteristics of 316L stainless steel manufactured by powder bed fusion laser beam**

Rasmus Gunnerek, Tatiana Mishurova, Giovanni Bruno and Eduard Hryha

Journal of the Japan Society of Powder and Powder Metallurgy, 2025

DOI:10.2497/jjspm.15B-T6-21

Paper III: **Improving productivity of low-alloy steels produced by powder bed fusion – laser beam**

Rasmus Gunnerek, William Hearn and Eduard Hryha

Manuscript

Paper IV: **Influence of microstructure and surface topography on material removal by the Hirtisation® process**

Rasmus Gunnerek, Gowtham Soundarapandiyan, Michael Christoph Doppler, Eduard Hryha and Uta Klement

Transactions of the IMF, 2024

DOI: 10.1080/00202967.2024.2411903

Paper V: **Chemical mechanical polishing of powder bed fusion – laser beam processed 316L stainless steel**

Rasmus Gunnerek, Gowtham Soundarapandiyan, Tatiana Misuhrova, Jakob Schröder, Giovanni Bruno, Joshua Boykin, Agustin Diaz, Uta Klement and Eduard Hryha

Manuscript

Paper VI: **Influence of build rate and post-AM surface treatments on fatigue life of powder bed fusion – laser beam 316L stainless steel**

Rasmus Gunnerek, Subhani Buddhika Kumarasinghe, Tatiana Misuhrova, Johan Moverare, Uta Klement and Eduard Hryha

Manuscript

Contribution to appended papers

Paper I: The author, in collaboration with the supervisors, planned and executed most of the experimental work and subsequent analysis. The author drafted the manuscript, which was then revised by the supervisors.

Paper II: The author planned experimental work with collaborators and supervisors and performed a major part of the experimental work and analysed the results. Tatiana Mishurova performed synchrotron x-ray computed tomography and 3D reconstructions. The author wrote the paper with co-authors.

Paper III: The author planned the experimental work in collaboration with supervisors and performed and analysed the results. The author wrote the paper with co-authors.

Paper IV: The author planned the experimental work together with supervisors/collaborators and performed most of the microstructure characterization and analysed the results. Planning and performance of post-AM surface treatments was assisted by Michael Christoph Doppler. The author wrote the paper with co-authors.

Paper V: The author planned and performed most of the experimental work and analysed the results. The strategy and execution of post-AM treatment was assisted by Agustin Diaz and Joshua Boykin. The acquisition of residual stress measurements and analysis was done by Jakob Schröder and Tatiana Mishurova. The author wrote the paper in collaboration with co-authors.

Paper VI: The author planned and performed most of the experimental work and analysed the results. The acquisition of X-ray computed tomography, and analysis was provided by Tatiana Mishurova. Fatigue tests and fractography were performed with assistance from Subhani Buddhika Kumarasinghe. The author wrote the paper in collaboration with co-authors.

Table of Contents

1. Introduction

1.1 Background

Powder bed fusion – laser beam (PBF-LB), a specific type of additive manufacturing (AM), presents a promising manufacturing route for the future fabrication of high-performance components. The ability to manufacture complex parts with reduced waste, the design freedom it offers, and its capacity to process a great variety of materials [1–3] are benefits that have driven significant interest across several industries. In sectors such as aerospace, biomedical, and energy, the customization and light weight achievable through PBF-LB can outperform conventionally manufactured components.

However, the high cost associated with the PBF-LB process remains a significant bottleneck where the low productivity has been consistently identified as a primary factor driving these high costs and hindering broader industrial uptake [4]. This low productivity is evident when comparing PBF-LB to conventional manufacturing methods, as the layer wise processing in PBF-LB typically exhibits low build rates. Also, the build volumes of PBF-LB machines are typically small, giving restrictions on the number of the components being printed, consequently driving the cost for each component. Figure 1 illustrates the cost per component for conventional manufacturing (CM) and PBF-LB with respect to lot size (Fig. 1a) and part complexity (Fig. 1b), highlighting their distinct economic advantages. CM achieves lower costs with larger lot sizes due to tool investments, making PBF-LB more competitive for small to medium volumes (Fig. 1a). However, CM cost per component increases with complexity, whereas PBF-LB cost remains relatively stable and allows for geometries beyond conventional methods (Fig. 1b) [5]. PBF-LB is therefore valuable for producing small to medium batches of highly complex parts. However, the necessity for post-processing to achieve desired specifications adds to the overall cost and lead time [6]. Consequently, significant research efforts are directed towards improving the productivity of PBF-LB, with a key focus on increasing in-process build rates to enhance its overall efficiency and economic viability.

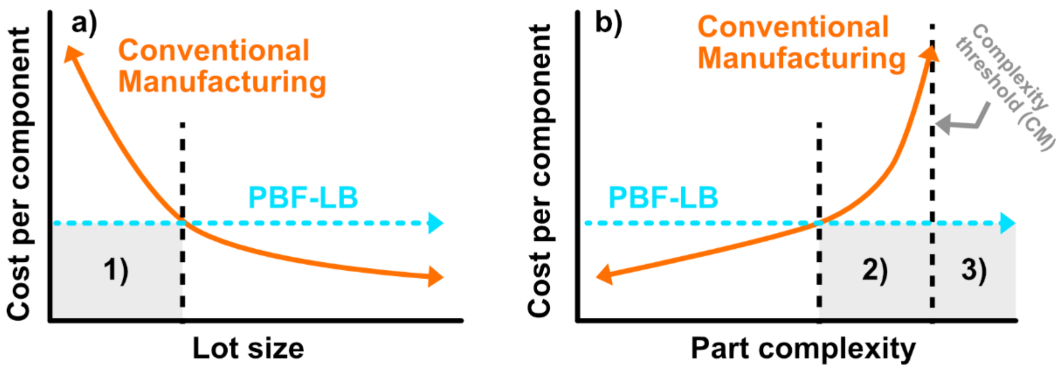

Figure 1: Cost per component comparison between conventional manufacturing and PBF-LB [5].

To increase build rates in PBF-LB, several strategies have been explored. One approach involves using multiple laser systems to shorten the layer exposure and consolidation time, though this introduces complexities like laser interaction [7]. Another key method is that build time can be reduced by scaling main printing parameters such as laser power, scan speed, layer thickness, and hatch distance. While combining increased values for these parameters can lower build time, it also presents significant challenges. These include the potential for increased porosity due to insufficient melting, degraded surface quality and altered microstructural evolution from modified thermal histories. Moreover, achieving high productivity without sacrificing the mechanical properties and overall integrity of the final parts requires careful optimization across these process parameters. Consequently, resolving these productivity issues, alongside the economic considerations of post-processing, is vital for broadening the application of PBF-LB to higher-volume and cost-sensitive industries.

A key aspect of addressing these challenges and expanding the applicability of PBF-LB lies in the selection and understanding of appropriate materials. Within this context, structural steels, such as low alloy steels, present an opportunity for cost-sensitive industries like automotive. These industries could benefit from the on-demand printing capabilities and shortened lead times offered by PBF-LB, particularly in the production of spare parts [8,9]. A major factor influencing the cost-effectiveness of PBF-LB is the duration of the printing process. Upscaling the primary printing parameters holds the potential to substantially reduce these costs. This approach, however, may come with a trade-off, potentially leading to a higher fraction of defects within the PBF-LB components. Additionally, the martensitic transformation can introduce further challenges, including cracking. Despite this potential increase in defects, it is important to note that many cast and powder metallurgy components currently used in the automotive sector can tolerate porosity levels of up to 5% [10]. Therefore, the critical challenge lies in thoroughly understanding the impact of both the fraction of porosity and its characteristic features on the resulting mechanical properties. Addressing these issues is vital to ensure the necessary process robustness and to facilitate the design of components that achieve the desired microstructure and properties.

While low alloy steels offer potential areas of application, 316L stainless steel stands out as one of the most extensively used and robust materials for PBF-LB due to its processability and the broad field of applications, supported by its exceptional corrosion resistance and mechanical properties [11]. Notably, compared to other as-built alloys processed via PBF-LB, including nickel-based superalloys, structural steels, and titanium-based alloys, 316L demonstrates notable static properties, exhibiting high ductility (above 40%) and yield strengths exceeding 550 MPa [12], positioning it as a highly mature alloy in PBF-LB, and thus a better benchmark alloy for this study.

To support the broader adoption of PBF-LB processed ferrous alloys, this thesis contributes to the understanding of the relationship between porosity and processing parameters in high-productivity PBF-LB manufacturing of low alloy steels and 316L stainless steel. The primary focus is on identifying how various process parameters influence pore characteristics, specifically pore size, shape, distribution, orientation, and overall fraction, as these factors directly affect mechanical performance. Additionally, the study examines how surface treatment methods can be employed to reduce surface roughness.

1.2 Research Objectives

To address these knowledge gaps and further the application of high-productivity PBF-LB for ferrous alloys, the following research objectives have been defined. The connection between the research questions and the appended papers are presented in Table 1.

RQ1: How do high-productivity process parameters in PBF-LB influence the pore characteristics of ferrous alloys?

RQ2: How do as-printed microstructure and surface roughness influence material removal during post-AM surface treatment?

RQ3: How do surface roughness and pore characteristics influence the fatigue strength of PBF-LB processed stainless steel?

Table 1. Connection between papers and the research questions investigated.

	RQ1	RQ2	RQ3
Paper I			
Paper II			
Paper III			
Paper IV			
Paper V			
Paper VI			

2. Powder Bed Fusion – Laser Beam

Additive manufacturing refers to the process of joining materials layer-by-layer based on three dimensional models. This offers unique possibilities of complex material production compared to conventional subtractive or formative manufacturing processes [13]. According to the ISO/ASTM 52900:2021 standard [14] processes are typically categorized into seven types based on the form of feedstock used and the method by which the material is joined. These include vat photopolymerization (VPP), material extrusion (MEX), sheet lamination (SHL), binder jetting (BJT), powder bed fusion (PBF), material jetting (MJT), and directed energy deposition (DED). As per the AMPOWER report 2025 [15], the AM market reached a total revenue of 10.72 billion euros in 2024 with an estimated market growth of 13% until 2029, corresponding to expected revenues in the order of 20 billion euros. Out of the AM categories the PBF-LB process stands for the major contribution of revenue and investment.

2.1 Principle of powder bed fusion – laser beam

Typical for most PBF-LB systems is that a high-energy laser source is used to selectively melt and fuse metallic powder within a powder bed, enabling the layer-by-layer creation of three-dimensional structures according to a CAD-file. This allows for the manufacturing of highly complex structures with greater geometric flexibility compared to traditional manufacturing techniques. Through its development, if process parameters are optimized, metal components close to full density (above 99.9%) are possible, reaching mechanical properties comparable or even better than conventional counterparts. The benefits to manufacture complex components with necessary performance on demand, with high material utilization and reduced lead times, have attracted a variety of industries such as medical, aerospace and automotive industry [16]. Another benefit is the ability to process a wide range of materials. For instance, stainless steels like 316L and 17-4PH provide excellent corrosion resistance for medical and chemical applications, while tool steels such as H13 have potential for manufacturing durable tooling [17]. Nickel-based superalloys, including Inconel 718, are important for high-temperature environments in aerospace [18]. Furthermore, lightweight yet strong aluminium alloys like AlSi10Mg find use in automotive and aerospace [19], and titanium alloys such as Ti-6Al-4V are valued for their biocompatibility in medical implants and high strength-to-weight ratio in aerospace [20]. Additionally, cobalt-chromium alloys serve in medical and dental fields due to their biocompatibility and wear resistance [21], and copper alloys are utilized for their conductive properties [21]. With its possibilities to produce very hard to manufacture metals, ongoing advancements continue to broaden the material possibilities for PBF-LB, enabling even wider industrial adoption of the process.

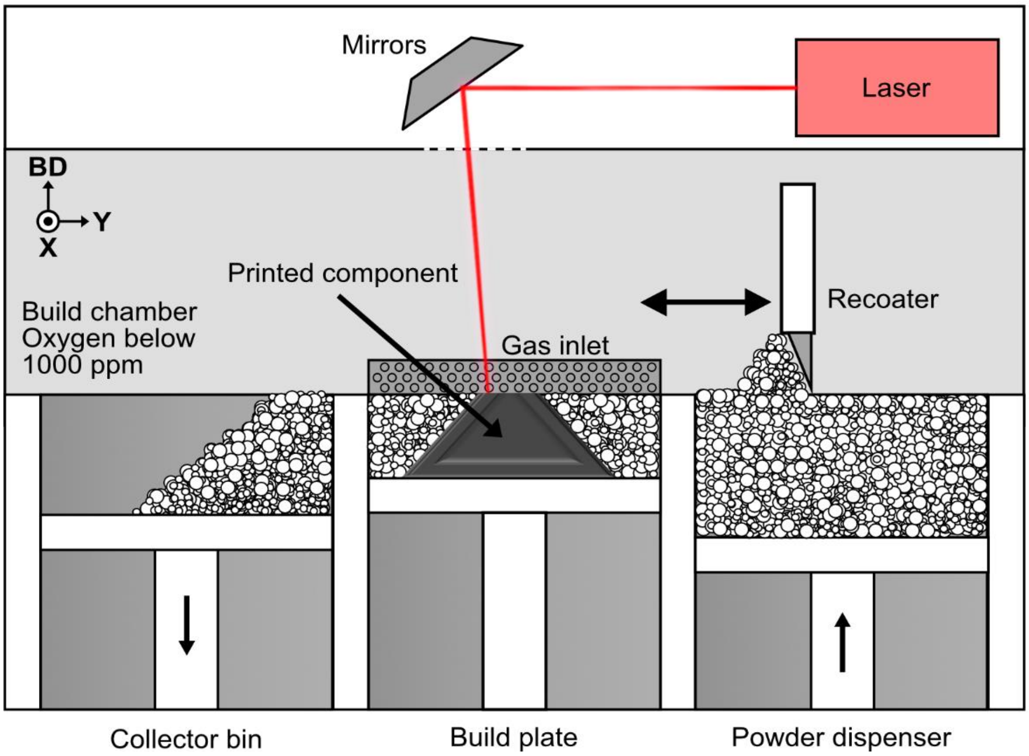

Figure 2: Illustration of the working principle of PBF-LB and its main components.

The main components and principle, typical of most PBF-LB machines, are presented in Figure 2. The setup resembles the EOS M290 by EOS GmbH, Germany, used in this thesis work. Sieved metal powder is loaded in the powder dispenser and distributed in thin layers on to the build plate by a recoater system. Based on pre-defined geometry, mirrors navigate a laser source of Gaussian distribution and spot size of ~85 µm. This provides localized melting and solidification along movement in the x- and y- axes. After each layer is completed, the build plate moves downward along the build direction (BD), allowing a new layer of powder to be spread across the surface. This cycle continues layer by layer until the full 3D geometry is completed [2]. The finished component is fused to the build plate and needs removal typically by wire electric discharge machining or band saw. Unused powder collected from the surrounding area and the collector bin can be recycled for future builds, contributing to efficient material usage. To minimize contamination and oxidation, the process is conducted in an inert gas environment, typically using argon, nitrogen, or helium [22], while maintaining the oxygen content below 1000 ppm. A continuous gas flow directed along the x-axis helps to remove spatter particles, thereby preventing them from settling on the powder bed or already solidified sections of the component.

2.2 Process parameters

The PBF-LB process involves a multitude of parameters, estimated around 100, that can affect the final part [6,23]. However, this thesis study narrows its focus to the key process parameters most critically linked to the build quality: laser power (p), scan speed (v), layer thickness (t), and hatch distance (h). Understanding the interplay of these parameters is crucial, as they dictate the dimensions and characteristics of the generated melt pool and melt tracks, the fundamental building units in the PBF-LB process, as depicted in Figure 3.

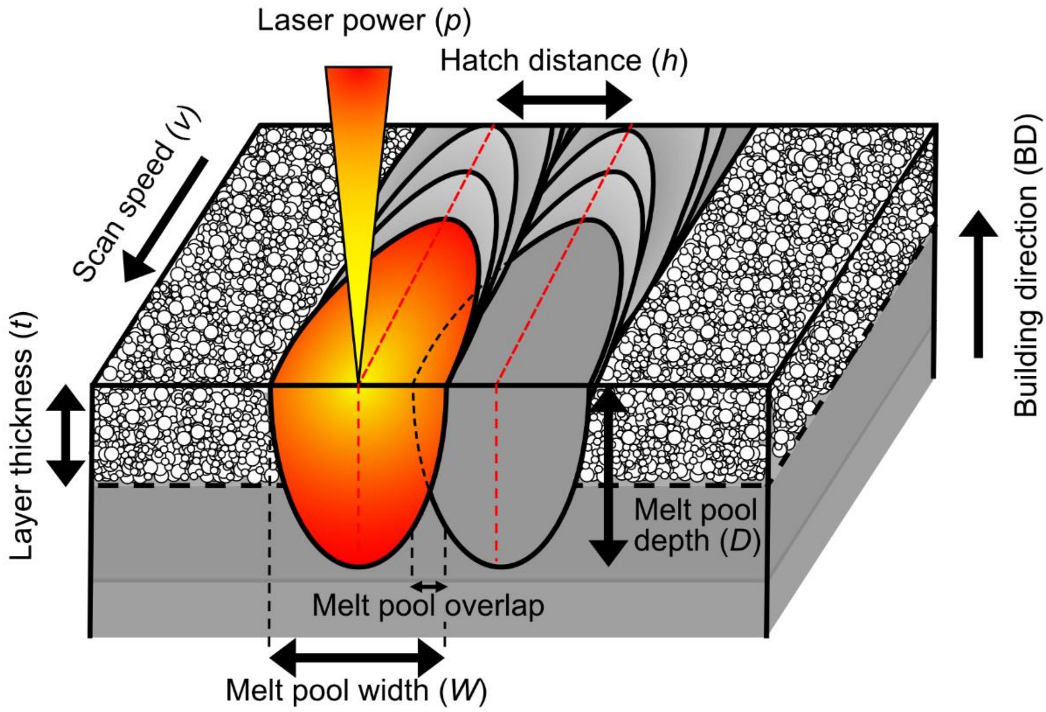

Figure 3: Schematic illustration of the PBF-LB process, depicting the main process parameters and their influence on the melt pool dimensions and overlap during the solidification of a layer.

2.2.1 Main printing parameters

The laser power is a critical parameter, directly governing the dimensions of the melt pool, specifically its depth (*D*) and width (*W*). Consequently, this determines the local temperature gradient within the powder bed. The laser power was limited to 400 W in the EOS M290 used in this work but can vary from 50 to 1000 W depending on the machine system [2]. Using adequate laser power is essential to ensure complete fusion and robust bonding between successive layers and adjacent melt tracks. Conversely, using excessive laser power can lead to undesirable effects like material evaporation and instabilities within the melt pool.

The velocity at which the laser beam crosses the powder bed surface is called the scan speed. This parameter, in conjunction with laser power and layer thickness, plays a crucial role in defining the melt pool geometry of individual melt tracks. Employing high scan speeds typically results in shallow and narrow melt pools, characterized by rapid solidification. Reducing the scan speed leads to the formation of deeper and wider melt pools and consequently slower solidification rates.

Following the laser scanning of a layer, the build platform is lowered by a predefined increment known as the layer thickness, dictating the amount of new powder deposited for the subsequent layer. Typically, layer thicknesses range from 20 to 100 µm, with the choice often dictated by the desired characteristics and productivity of the final component [24,25]. Utilizing finer layers generally results in higher geometrical accuracy and smoother surface finishes. Ensuring adequate layer thickness is crucial for achieving proper metallurgical bonding with the previously solidified layer, requiring a melt pool depth that exceeds the selected layer thickness.

Proper overlap between adjacent melt tracks, defined by the hatch distance, is essential for achieving dense and homogeneous PBF-LB parts. The optimal hatch distance is not fixed but is influenced by other parameters, notably layer thickness and scan rotation. A finer layer thickness, for instance, can enhance remelting and compensate for potential defects, thereby impacting the ideal hatch distance [25].

2.2.2 Energy input

To gain a simplified understanding of the connection between printing parameters and resulting material properties, combined parameters representing the energy input are often employed and assessed through parameters such as achieved density, microstructural features, and mechanical performance [3]. The simplest among these parameters is the linear energy density (LED), expressed in J/mm (Eq. 1), which depends only on laser power and scan speed. LED represents the energy delivered per unit length and is frequently used in fundamental studies to assess the stability and characteristics of individual melt tracks [26].

$$LED = \frac{p}{v} \left(\frac{J}{mm}\right) \tag{1}$$

Expanding on this concept, the surface energy density (SED), measured in J/mm² (Eq. 2), is obtained by adding the hatch distance to the LED equation. Research has shown that SED yields a decent correlation with melt pool dimensions, specifically its depth and width [27,28]. Furthermore, SED has been used to assess the overlap between neighbouring melt pools within a single layer [6], and studies have demonstrated a good correlation between SED and process windows for achieving desired material properties such as hardness, density, microstructure, and the presence of specific phases [29].

$$SED = \frac{p}{v \cdot h} \left(\frac{J}{mm^2}\right) \tag{2}$$

Finally, the volumetric energy density (VED), measured in J/mm³ (Eq. 3), represents the energy imparted per unit volume and incorporates laser power, scan speed, hatch distance, and layer thickness. VED is widely utilized to indicate optimum ranges for these main printing parameters to achieve desired performance outcomes, such as density, microstructure, and mechanical properties. However, it is important to note that VED offers a simplified view and does not fully capture the complex mass and heat transfer phenomena within the melt pool [30]. Therefore, VED should be used primarily as an indication of processability as for the previous mentioned SED and LED.

$$VED = \frac{p}{v \cdot h \cdot t} \left(\frac{J}{mm^3}\right) \tag{3}$$

2.2.3 Scanning strategies

So far, the main printing parameters governing the formation of individual melt tracks in the PBF-LB process have been discussed. However, the arrangement and execution of these melt tracks on a larger scale can be controlled by employing different kinds of scan strategies and patterns, which alter the path of the scan vector. This has a great impact on defect mitigation, surface roughness, residual stress, and the microstructure of the produced parts.

Scanning patterns

In PBF-LB, there is a separation between contour and hatch/infill parameters, where contour refers to any scanning performed at the outer surface, and the hatch pattern refers to any strategy employed in the bulk of each layer [31]. Common hatch patterns include the meander pattern, where the laser scans the entire cross-section of the part in a continuous, back-and-forth motion along parallel lines. In contrast, the stripe pattern divides the cross-section of the part into smaller, more manageable individual stripes, each with a defined stripe width, that the laser follows. Within these hatch patterns, the direction of the laser movement is crucial. The laser can move back and forth along adjacent lines, referred to as bidirectional scanning, see Figure 4. Alternatively, the laser can consistently move in one direction for each line before stepping to the next, which is unidirectional scanning. However, this has shown to lead to larger anisotropic residual stress distributions [32].

Scan rotation

Beyond the scan patterns that define the distribution of scan vectors within each layer, the scan rotation strategy plays a role in determining the homogeneity of the resulting surface and microstructure. A 67° scan rotation is often preferred as it maximizes the number of layer rotations required before the scan vectors return to their initial orientation. This frequent change in direction helps to create a more homogeneous build. On the contrary, a 0° scan rotation, where scan vectors remain aligned between successive layers, forces the start and end points of melt tracks to occur along the same axis throughout the build. This consistent alignment has been shown to induce anisotropic residual stresses [32], variations in microstructure [33], and affects the resulting surface topography [34]. The differences between 0° and 67° scan rotation are highlighted in Figure 4, where the bottom part of the image illustrates how 0° scan rotation leads to anisotropy on the different faces of the cube (see Fig. 4a and 4b).

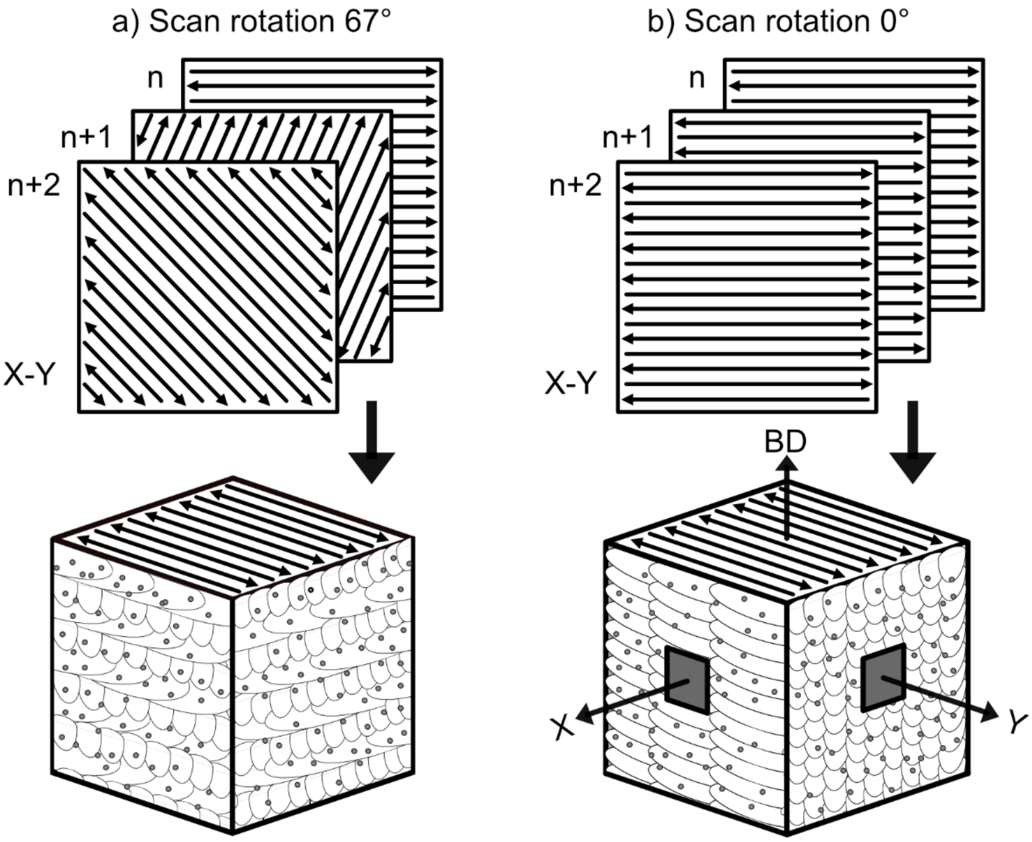

Figure 4: Schematic illustrating the difference in scan rotation strategies used in PBF-LB. Here a) shows the state-of-the-art 67° scan rotation between successive layers, while b) depicts a 0° scan rotation adapted from [34]. The arrows indicate the laser scan direction within each layer.

2.3 Characteristics of as-built components

This section details the unique characteristics of PBF-LB materials that significantly influence the performance of manufactured parts. As previously mentioned, defects often compromise the quality and structural integrity of PBF-LB components. These flaws arise from a complex interplay of factors inherent to the process, including the material properties, the energy input, the processing atmosphere, and the specific process parameters discussed in earlier sections. Building on this foundation, this section will now examine common defects encountered during PBF-LB printing, focusing on the clear link between their formation and the process inputs, particularly the role of process parameters.

2.3.1 Porosity

Defects can manifest at various stages of the process, with porosity being a prevalent type. Porosity can be broadly categorized as either process-induced or originating from the powder feedstock. In this context, focus will be on process-induced porosity, which arises from the interaction of printing parameters such as laser power, scan speed, hatch distance, and layer thickness. As illustrated in Figure 3, the combination of these parameters dictates the melt pool and melt track geometry. During PBF-LB, achieving a stable, semi-spherical melt pool geometry through conduction mode melting [35] is desirable. Deviations from this stable morphology, often resulting in an elongated melt pool and a transition to keyhole melting mode due to specific parameter combinations, can lead to porosity formation. This section will explore the intricate relationship between process parameters, the resulting melt pool geometry, and how these interactions induce different types of porosity.

Lack of fusion

Lack of fusion typically referred to as (LoF) porosity arises when the energy input during the PBF-LB process is insufficient (low VED) to achieve proper cohesion between solidified layers or adjacent melt tracks, as illustrated in Figure 5. Insufficient penetration of shallow melt pools into previously built layers leads to LoF between layers referred to as inter-layer porosity. This results in large, irregularly shaped, and elongated pores oriented perpendicular to the build direction (Figure 5a) [3]. Similarly, inadequate overlap between subsequent melt tracks also causes LoF (inter-hatch porosity), but the resulting pores tend to be aligned parallel to the build direction and can extend across multiple layers (Figure 5b) [36]. Compared to other types of porosity, LoF pores are distinguished by their sharp and irregular morphology. These features can act as stress concentration sites, promoting crack initiation under mechanical loading and consequently reducing the mechanical performance of PBF-LB components. Therefore, optimizing process parameters to minimize the occurrence of LoF porosity is crucial.

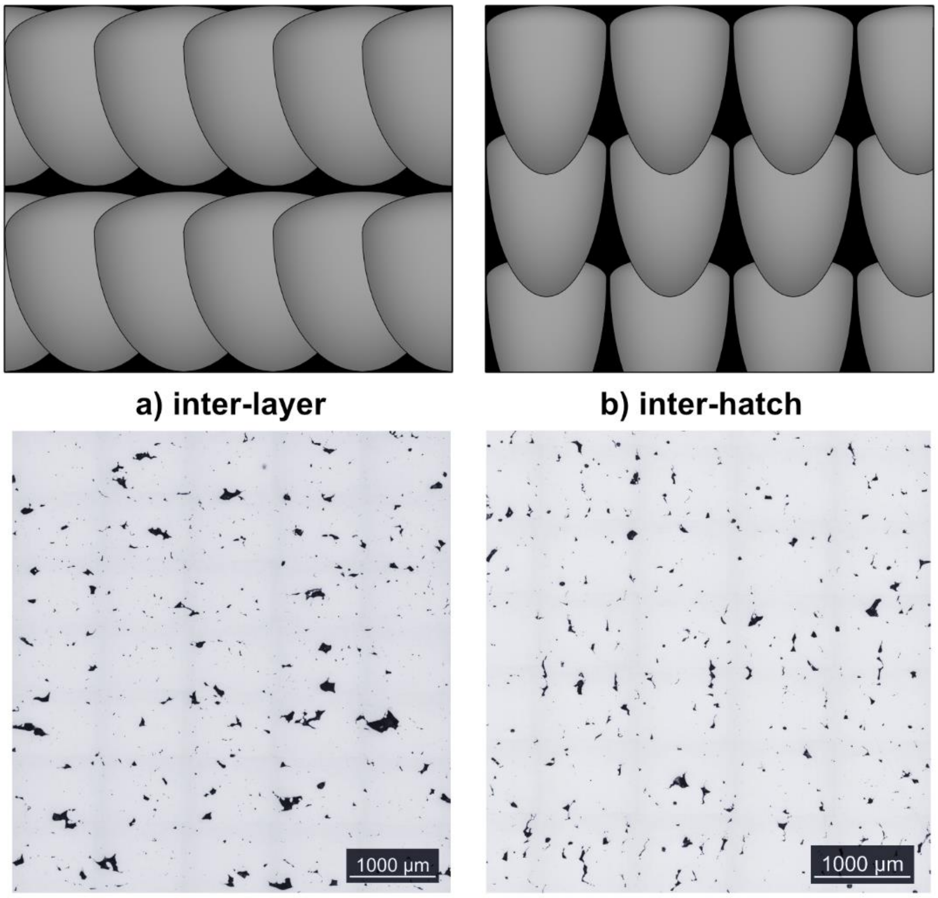

Figure 5: Simplistic view of porosity resulting from a) LoF between layers (inter-layer) and b) insufficient overlap between neighbouring melt tracks (inter-hatch). The bottom row shows a micrograph of how these defects look for 316L stainless steel.

Keyhole porosity

Elevated energy input during PBF-LB, often achieved through low scan speeds and high laser power (resulting in high VED), can induce a transition from a stable conduction melting regime to a keyhole melting regime. Keyhole mode melt pools are characteristically deep and narrow, leading to steep local thermal gradients. Under these conditions, the vaporization of metal generates significant recoil pressure that acts downwards within the melt pool [37]. The combination of this pressure and the constricted geometry of the keyhole can hinder the escape of vaporized metal from the bottom, resulting in the formation of semi-spherical pores in the solidified material [35–38]. As depicted in Figure 6, the melt flow within the keyhole and the keyhole movement are highly dynamic over short time scales. The clockwise flow of the melt behind the keyhole, and the vertical movement ahead of it, create instabilities along the keyhole boundary, leading to necking (I-II). This narrowing of the keyhole restricts energy delivery, causing the bottom to solidify as it is overtaken by the solidifying front (II). Ultimately, when the keyhole solidifies at the liquid-solid interface, a keyhole pore is left behind in the microstructure (III). Strategies to reduce keyhole porosity include decreasing laser power or increasing scan speed to lower the energy input. Nevertheless, the spherical nature of keyhole pores (Fig. 6a and Fig. 6b) generally makes them less detrimental to the mechanical performance of the material compared to LoF defects [39].

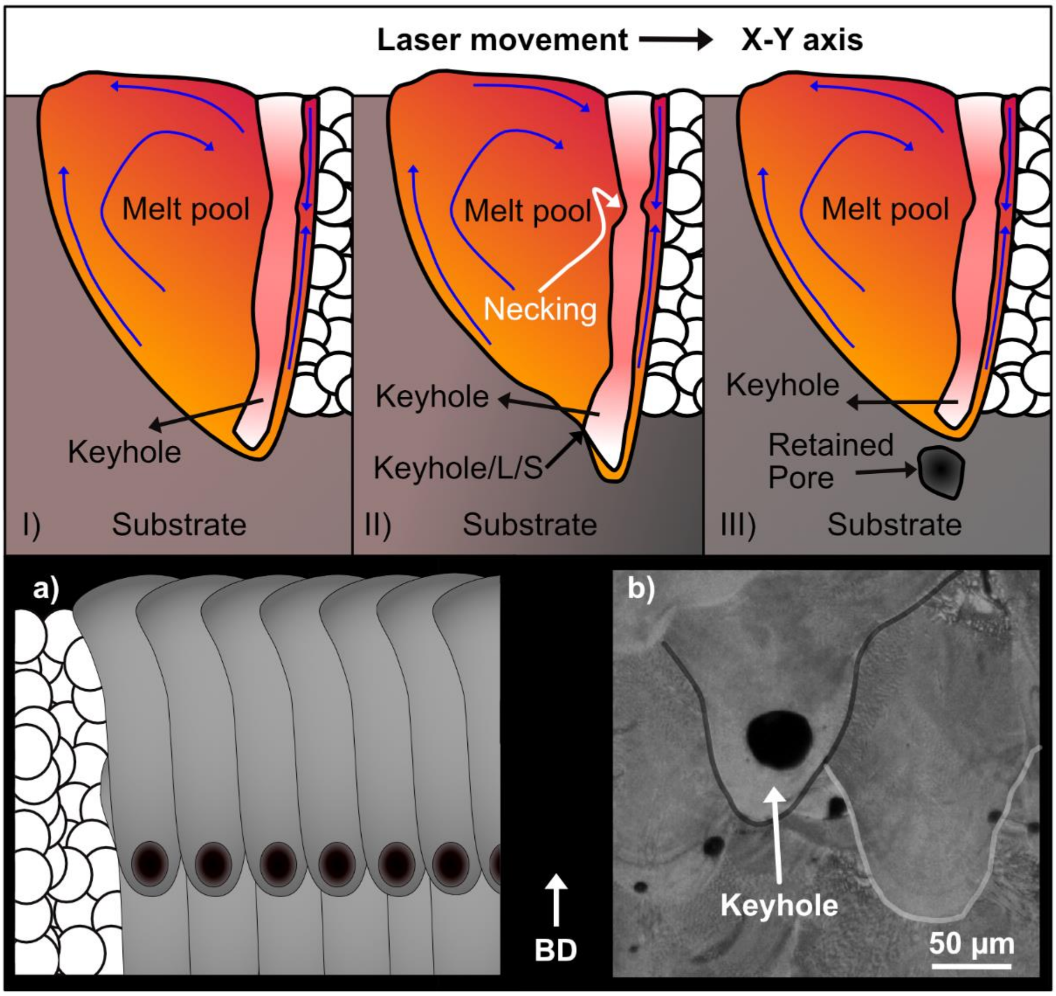

Figure 6: I) - III) the sequence of mechanisms leading to keyhole pore formation, along with the intricate dynamics within the melt pool, as inspired by [35]. Keyhole porosity a) simplified view and b) etched micrograph of 316L stainless steel viewed in the build direction (BD).

Gas porosity

Gas atomization is a prevalent method for producing the powder feedstock utilized in PBF-LB. In this technique, a high-velocity stream of inert gas is directed at a flow of molten metal, which disintegrates into droplets. These droplets subsequently solidify into spherical particles as they interact with the surrounding gas. The rapid cooling inherent in this process can lead to the entrapment of small pores, typically less than 10 µm in diameter, within the powder particles. This is referred to as gas porosity [38,40]. Although the PBF-LB process often diminishes the extent of this porosity, some residual gas pores may persist in the final material. Given their limited size and spherical morphology, these remaining pores are generally not viewed as having a substantial negative impact on mechanical properties [37,38].

Spatter

In PBF-LB processes, the intense and dynamic environment within and surrounding the melt pool can lead to the ejection of metal droplets or powder particles across the powder bed, a phenomenon referred to as spatter. Based on their formation mechanism, spatter can be broadly classified into cold and hot spatter [41]. Hot spatter originates from recoil pressure-induced instabilities within the melt pool, while cold spatter is primarily driven by the interaction and entrainment of particles with the process gas flow [41,42]. These ejected spatter particles can negatively impact the printing process in several ways. Notably, the presence of spatter can lead to the formation of large LoF pores within the microstructure.

2.3.2 Surface roughness

While much attention has been directed towards understanding and mitigating bulk defects, the characteristics of their as-built surfaces present a similar complexity. The surface formation in PBF-LB is a highly dynamic process where the selective melting and rapid solidification by the laser leads to adherence of surrounding powder particles (Figure 7) to the component surface, resulting in a distinctive and irregular surface topography [43].

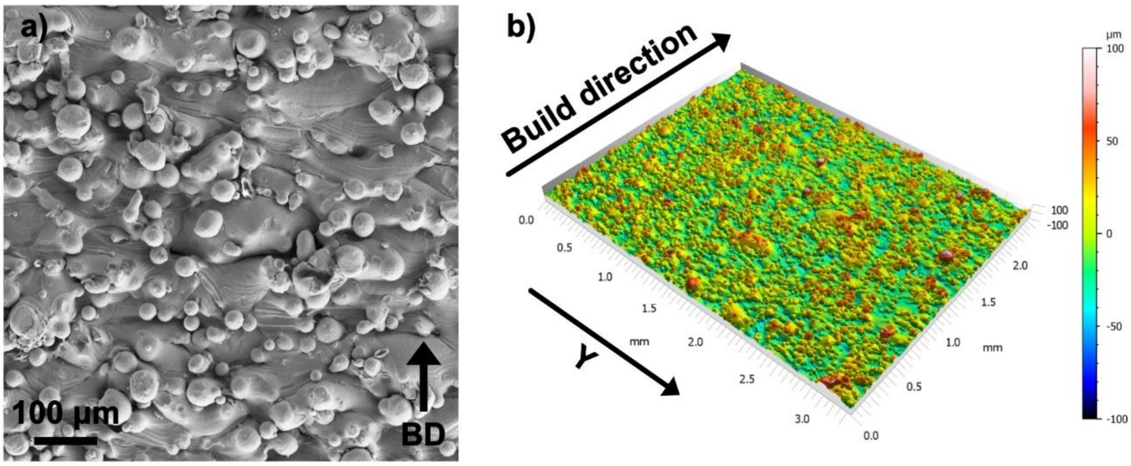

Figure 7: a) SEM image showing as-built surface topography. (b) 3D surface plot of the same area, obtained using optical profilometry.

Furthermore, the lower thermal conductivity of the powder compared to the solidified metal introduces variability in heat dissipation as the part geometry evolves along the build direction. This variation in heat flow can influence both the local microstructure [44,45] and the resulting surface topography [43]. The SEM micrograph (Fig 7a) shows powder adhered to the surface and a waviness generated by the melt pools and a 3D surface plot (Fig. 7b) of the same area using optical profilometer which shows variations in height across the surface.

Consequently, as-built components typically exhibit a relatively high surface roughness (Ra ~3 to 50 µm) [46], requiring post-processing for many applications, particularly those subjected to dynamic loads [47]. The well-established link between increased surface roughness and a higher propensity for crack initiation under fatigue loading directly impacts the service lifespan of components. However, it is important to note that this roughness can be mitigated to some extent through the optimization of process parameters. For example, the application of a contour parameter (as discussed in section 2.2.3), which scans the outer surface of the part, can effectively smoothen the melt pool boundaries and reduce powder adhesion, thereby improving the surface finish [48,49]. Therefore, while post-processing is often required, parameter optimization plays a role in minimizing the initial surface roughness.

2.3.3 Residual stresses

Another important factor influencing the integrity of PBF-LB components is residual stress, which refers to internal stresses existing within a material without external loads applied. These stresses operate in equilibrium at different length scales within a component, categorized into types I-III. Type I stresses (macro-stresses) act over long distances, comparable to the part size, and are often a consequence of the manufacturing process, arising from the steep thermal gradients inherent in PBF-LB, post-processing treatments like heat treatment or machining, and non-uniform plastic deformation. Type II stresses (micro-stresses) are more localized, finding equilibrium between individual grains and making them highly sensitive to the material microstructure and crystallographic anisotropy. Even smaller length scales, type III residual stress (sub-microstresses) are associated with lattice imperfections such as dislocations or other defects within the crystal structure [50]. The rapid, localized melting and solidification inherent to the PBF-LB layer-by-layer process, with solidification rates in the order of 10^5-10^8 $°C \cdot s^{-1}$ [51], induces significant thermal gradients that inevitably generate substantial residual stress in the resulting parts [50]. These stresses can severely compromise part functionality by leading to detrimental consequences such as cracking, significant distortion, and reduced dimensional accuracy, which highlights the necessity for effective stress management in PBF-LB manufacturing [52].

2.3.4 Microstructure

The typical microstructure of materials produced by PBF-LB is characterized by a unique set of features arising from the rapid solidification and thermal gradients inherent to the process, as discussed throughout this section regarding defect formation and surface characteristics. Often, a fine-grained microstructure forms due to the high cooling rates [53]. However, this can be anisotropic, with elongated grains or columnar structures oriented along the build direction. The layer-by-layer fabrication process, which contributes to the formation of inter-layer LoF porosity due to insufficient remelting as highlighted in Section 2.3.1, also imparts a distinct melt pool morphology, visible as overlapping, semi-elliptical regions when viewed in cross-section. Within these melt pools, influenced by the energy input from process parameters (Section 2.2.2), segregation of alloying elements can occur, leading to micro-segregation patterns [54]. The rapid solidification can also result in the formation of metastable phases or supersaturated solid solutions, which may differ from conventionally manufactured counterparts. The complex thermal history experienced by each layer, involving repeated heating and cooling cycles as subsequent layers are deposited, can contribute to the development of residual stresses (Section 2.3.3) and a hierarchical microstructure with variations in grain size and phase distribution across different layers. Furthermore, the presence of any residual porosity, whether LoF or gas entrapment (as detailed in Section 2.3.1), will also be a defining characteristic of the microstructure. Overall, the PBF-LB microstructure is a direct consequence of the intricate interplay between the applied process parameters and the inherent solidification behaviour.

2.4 Mechanical properties

The static mechanical properties of PBF-LB manufactured materials, such as tensile strength, yield strength, and ductility, are inherently linked to the microstructural features and the presence of defects discussed in the previous section. The fine-scale nature of microstructure often observed in PBF-LB materials can contribute to higher strength compared to conventionally manufactured counterparts. However, the anisotropy in grain structure, particularly the presence of columnar grains aligned with the build direction, can lead to direction dependent mechanical properties. Furthermore, the presence of porosity, especially LoF defects with their irregular shapes and sharp edges acting as stress concentrators, can significantly reduce the effective load-bearing area and promote premature failure under static loading. The specific process parameters employed during manufacturing play a crucial role in dictating the resulting density and microstructure [54], thereby directly influencing the achievable static strength and ductility. Subsequent heat treatments can be applied to modify the microstructure, reduce residual stresses, and potentially improve the overall static mechanical response.

Beyond static loading, the performance of PBF-LB components under cyclic loading conditions, or fatigue, is important for many engineering applications. The fatigue behaviour is particularly sensitive to surface quality and the presence of internal defects [47]. The inherent surface roughness of as-built PBF-LB parts, characterized by adhered powder and a wavy topography resulting from the layer-by-layer solidification, provides numerous potential crack initiation sites under cyclic stress. Similarly, internal defects such as porosity, particularly LoF pores with their sharp, irregular morphology, can act as critical stress concentrators, accelerating crack initiation and propagation, ultimately leading to reduced fatigue life. The orientation and distribution of these defects, which are strongly influenced by the process parameters and build strategy, play a significant role in determining the fatigue performance. Post-processing techniques, such as surface treatments and hot isostatic pressing (HIP), are often employed to mitigate the detrimental effects of surface roughness and internal porosity, thereby enhancing the fatigue resistance of PBF-LB manufactured components [55].

3. Productivity in PBF-LB

Achieving the desired characteristics in PBF-LB components, as detailed in previous sections, often involves careful optimization of process parameters. However, enhancing the productivity of PBF-LB presents a significant challenge: how to increase build rates without compromising these critical characteristics, or alternatively, how to design components to be more tolerant to them. The limitations in the production speed of PBF-LB stand as a considerable barrier to its widespread industrial application and overcoming this requires strategies that address both speed and quality.

3.1 Strategies to improve build rate

While various methods exist to improve the economic viability of PBF-LB, including increasing build speed through multi-laser systems or enhancing build volume with larger machines for simultaneous production, this study focuses on a more constrained approach. Specifically, it investigates how productivity, in terms of build speed, can be increased within the hardware limitations of the EOS M290 machine used in this thesis. For clarity, this investigation does not consider other factors that contribute to the overall cost of a PBF-LB component, such as expenses related to build preparation, operator time, material consumption and shielding gas usage [56]. However, the strategies presented are applicable to a wide range of commercial PBF-LB platforms.

Total build time in PBF-LB can be broadly divided into two main components: (1) the time spent consolidating the bulk material, and (2) the inter-layer time which includes platform movement and powder recoating. The bulk consolidation phase governed by scan speed, hatch distance, and layer thickness is typically the most time-intensive part of the process. These three parameters are therefore central to overall productivity. The build rate, defined as the volume of material processed per unit time (cm³/h), is primarily determined during the laser scanning phase (Eq. 4).

$$\text{Build rate} = v \cdot h \cdot t \; \left(\frac{cm^3}{h}\right) \tag{4}$$

Increasing the layer thickness reduces the number of layers required for a given part height, thereby lowering the total build time. This makes layer thickness an influential parameter in efforts to reduce production time and cost in PBF-LB [4,57]. While typical builds use layer thicknesses between 20 µm and 40 µm to achieve high density (Section 2.2.1), recent studies have demonstrated that layer thicknesses up to 120 µm can significantly improve productivity without sacrificing part quality [58].

To illustrate this, a demonstrator hydraulic block was fabricated using an 80 µm layer thickness of 316L stainless steel (Figure 8). The build achieved near-full density at a build rate of 28.8 cm³/h. As shown in Table 2, this corresponds to an approximate 75% reduction in total build time compared to the same part built at 20 µm, and around a 51% reduction compared to 40 µm. However, it is important to note that increasing the layer thickness also increases the risk of inter-layer LoF porosity, as discussed in Section 2.3.1.

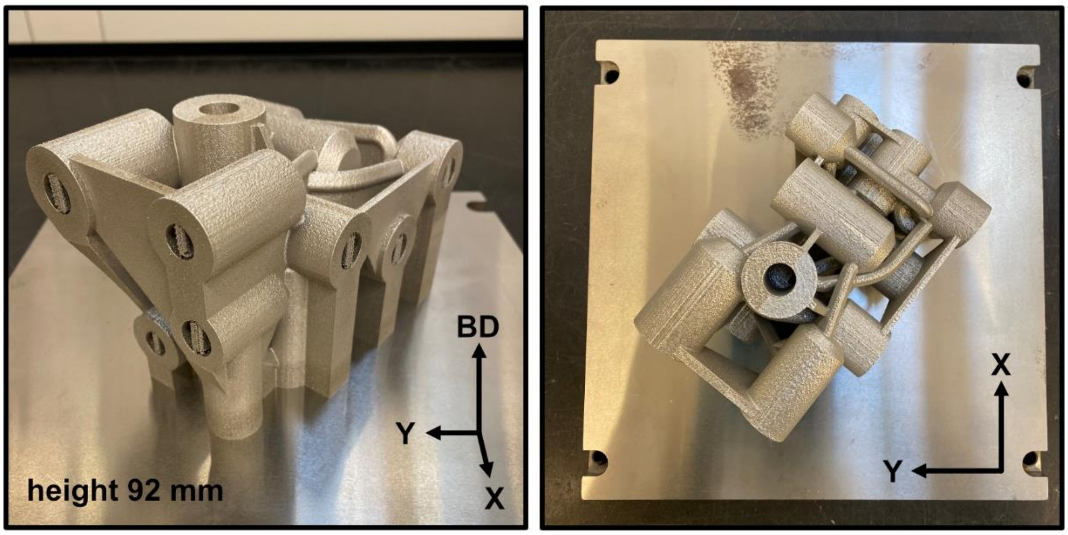

Figure 8: Demonstrator part produced with in the frame of "3D action" project printed with focus on high productivity using 80 µm layer thickness in 316L stainless steel.

Table 2: Build time required to produce demonstrator part presented in Fig. 8.

Layer thickness (µm)	Build rate (cm^3/h)	Build time (h)	Exposure time (h)	Recoating time (h)
20 µm	7.2	84	72	12
40 µm	13.3	43	37	6
80 µm	28.8	22	19	3

While increased layer thickness, as shown in Table 2, effectively reduces total build time, further improvements in productivity can be achieved by tuning hatch distance and scan speed. As illustrated in Figure 9, for a fixed build rate of 36 cm^3/h, the total build time varies depending on the selected parameter combination and the surface-to-volume ratio (S/V) of the part (0.14 – 2.12), calculated for a simple prism divided into smaller sections using EOSprint2.8 software.

For geometries with higher S/V, such as thin-walled or ribbed structures, increasing the hatch distance leads to more reduction in build time compared to increasing scan speed. This is primarily due to its stronger influence on exposure time at same build rate, as a larger hatch distance reduces the number of laser scan vectors required per layer. In contrast, increasing scan speed results in comparatively smaller reductions in exposure time, particularly for geometries with high surface complexity. As the figure demonstrates, total build time can be shortened by several hours through optimized hatch distance selection in high S/V cases. This highlights the importance of considering part geometry [59] when selecting process parameters, with hatch distance, scan speed, and layer thickness all contributing to exposure time a critical factor for achieving time-efficient builds in PBF-LB.

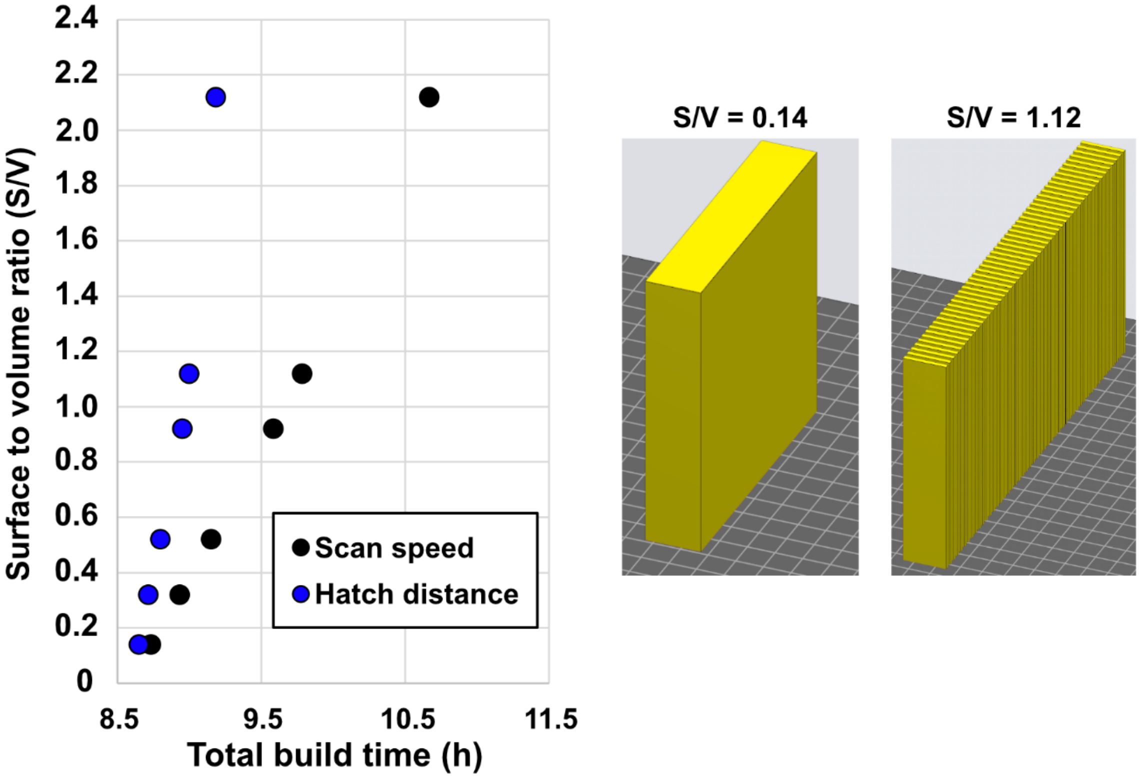

Figure 9: Estimated total build time as a function of surface-to-volume ratio (S/V) for a fixed build rate of 36 cm^3/h, comparing two parameter strategies: increased hatch distance vs. increased scan speed. S/V was varied by progressively subdividing a simple rectangular prism into thinner-walled sections, calculated in EOSprint2.8. The results show that for geometries with higher S/V, increasing hatch distance more effectively reduces exposure time.

Beyond the primary parameters discussed, other process-related factors need consideration when aiming to improve the build rate in PBF-LB. For instance, scan strategies such as stripe versus meander patterns (discussed in section 2.2.3) can influence both scan time and thermal management across larger cross-sections [60]. Additionally, the use of contour scans typically applied to improve surface finish [61] introduces extra laser passes, thereby increasing exposure time. While necessary in applications where surface quality is critical, the inclusion or exclusion of contour scans can present a trade-off between surface roughness and build productivity [62]. Furthermore, the efficiency of laser path planning, often governed by the machine control software, can affect non-productive movements and idle times during scanning [60]. These factors, although secondary to the main build rate parameters, collectively contribute to the overall efficiency of the process and should be considered when developing strategies for high-productivity manufacturing.

Given the significant impact of the primary printing parameters, this thesis focuses specifically on layer thickness, scan speed, and hatch distance as the main variables for increasing build rate. However, while these parameters can substantially reduce build time, it is essential to evaluate how such changes affect the quality of the as-built components, both in terms of internal integrity and surface condition.

3.2 Challenges associated with increased productivity

While increasing build rates offers the potential for enhanced productivity, this often comes at the expense of part quality, leading to increased surface roughness and fraction of internal defects. As previously discussed, the VED (Eq. 3) dictates the energy input into the powder bed. Because build rate is directly influenced by scan speed, hatch distance, and layer thickness, increasing it requires a reconsideration of the entire set of process parameters. Otherwise, increases in layer thickness, while the most effective way to boost the build rate, will inherently lead to a decrease in VED, assuming laser power remains constant. This reduction in energy increases the risk of the formation of LoF pores. To counteract this effect at higher build rates and maintain adequate melting, a new set of process parameters needs to be developed to ensure required remelting between the layers and melt tracks. However, common PBF-LB systems often have limitations when it comes to laser-based process parameters as e.g. laser maximum laser power, laser focus, energy distribution etc., limiting the extent to which high-build rate process parameters can be developed.

However, the impact of these defects on mechanical properties is not solely determined by their volume fraction but also by their characteristics, such as shape, morphology, and orientation. For instance, Choo et al. [63] demonstrated the significant influence of LoF pore orientation on tensile properties. The findings indicated that when the major axes of these pores were aligned parallel to the loading direction, the impact on static properties remained minimal even at a relatively high porosity level of 1.8%. Similarly, Gong et al. [64] investigated the effect of defect type on the static and fatigue properties at porosity levels of 1% and 5%. Their study revealed that keyhole porosity up to 1% had little effect on tensile strength, although elongation to fracture was significantly reduced at 5% porosity. In contrast, comparable levels of LoF porosity resulted in more severe reductions in both elongation to fracture and tensile strength. Thus, while increased build rates can lead to higher porosity and reduced static properties, the specific type and morphology of the pores play a role. A thorough understanding of these characteristics, and how they relate to the chosen process parameters, is essential for tailoring builds to maintain acceptable mechanical performance even under high-productivity conditions.

Compared to static properties, the fatigue behaviour of PBF-LB components is even more sensitive to surface and subsurface defects. The inherently rough surfaces of as-built parts, as discussed in Section 2.3.2, tend to worsen at higher build rates. Larger layer thicknesses can increase surface roughness due to more pronounced melt pool topography and the presence of partially fused powder particles. Furthermore, the staircase effect becomes more apparent, particularly on inclined or curved surfaces [65]. These surface irregularities act as significant stress concentration sites, promoting crack initiation and severely impacting fatigue life. To mitigate these issues, post-processing methods such as machining are frequently employed. However, these treatments add cost and may not be suitable for complex geometries, thereby challenging the near-net-shape benefits of PBF-LB.

3.3 Strategies to improve surface roughness

As discussed in Section 3.2, the inherently rough surfaces of as-built PBF-LB components can significantly compromise fatigue life by serving as stress concentrators and crack initiation sites. Therefore, effective surface treatment is essential not only for improving the visual and dimensional quality of parts but also for enhancing their mechanical performance, particularly under cyclical loading. The need to reduce surface roughness is especially pressing in high-productivity builds, where process parameters often lead to increased surface irregularities due to a less stable process environment.

Achieving satisfactory surface finishes on PBF-LB parts, especially those with intricate geometries, remains one of the key post-processing challenges [66]. Traditional surface treatments like machining are often limited by accessibility, particularly for internal or fine-featured structures [67,68]. Moreover, even highly optimized process parameters during printing cannot fully eliminate surface roughness [48]. As a result, the development and adoption of novel surface finishing techniques are critical for unlocking the full potential of PBF-LB in industrial applications [69–71]. To address these challenges, promising surface treatment technologies were recently developed, including Hirtisation® [72] and chemical mechanical polishing (CMP) [73], both of which offer capabilities beyond those of conventional finishing methods.

Hirtisation® utilizes chemical and electrochemical mechanisms to remove material and can access both external and internal surfaces (Figure 10). This makes it highly suitable for parts with high complexity. The process effectively removes loosely sintered powder and smooths irregularities while preserving the integrity of geometrical features. Studies focusing on 316L stainless steel have indicated that Hirtisation® can reveal underlying grain boundaries in solution-annealed conditions [74]. However, more research is required to understand how variations in surface microstructure influence material removal behaviour during this treatment. Since the surface condition and microstructural variations in PBF-LB are highly dependent on factors such as scanning strategy and component design, post-processing methods like Hirtisation® must be evaluated within this context to ensure consistent and effective results.

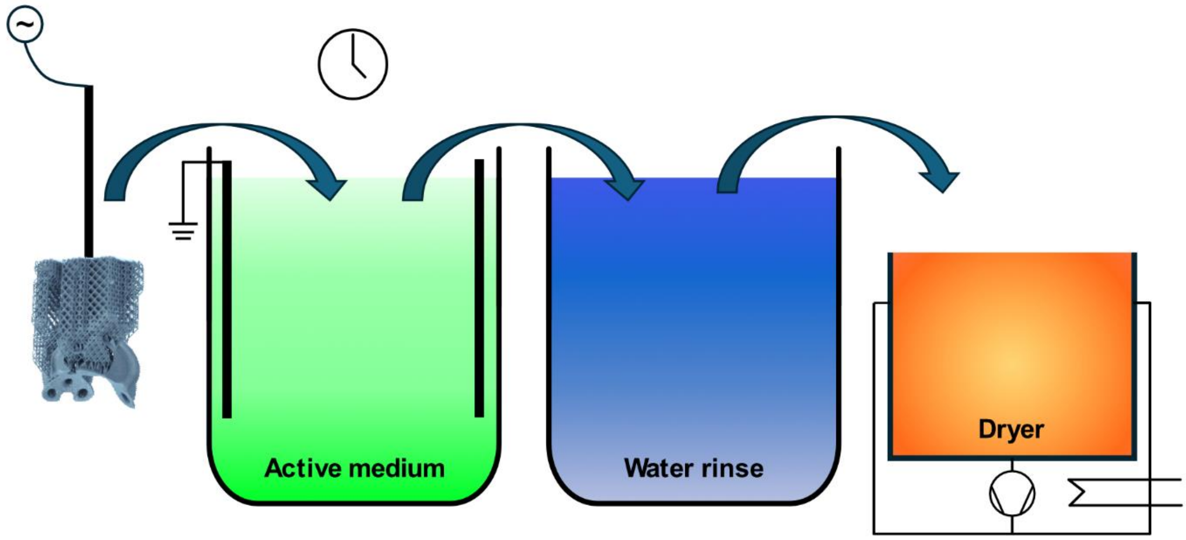

Figure 10: General workflow for Hirtisation® with one active step. The part is contacted and immersed in the active medium, where material is removed over time. When the target condition is achieved, the part is rinsed and dried; adapted from [34].

In addition to other surface modification techniques, chemical mechanical polishing (CMP), developed by REM Surface Engineering [75], also referred to as chemically accelerated vibratory finishing (CAVF), has emerged as a promising method for improving surface quality. CMP operates through a synergistic mechanism involving chemical activation of the surface and mechanical interaction with non-abrasive media while components are placed in a vibratory bowl. This approach allows for selective removal of surface peaks while preserving underlying features, as the chemical agent forms a temporary monolayer that is easily displaced by gentle mechanical rubbing. The method has demonstrated effectiveness across various alloys, including steels, titanium, copper etc. Studies report substantial reductions in surface roughness (Ra < 0.1 µm), enhanced uniformity, and improved resistance to corrosion, all achieved without inducing significant changes in the material microstructure [76]. Despite these advantages, further research is needed to fully understand how parameters such as scan strategy, build orientation, and the initial condition of the surface influence the performance and outcome of CMP treatments.

The effectiveness of surface treatments such as Hirtisation and CMP depends on a clear understanding of the required depth of material removal. The PBF-LB often produces surfaces with varying defect types, including subsurface porosity, partially fused particles, and layer-induced waviness. These features can differ significantly based on scan strategy, build orientation, and processing parameters. If material removal is insufficient, critical defects may remain. Furthermore, excessive removal, on the other hand, risks altering part geometry or exposing deeper flaws [77]. Accurately characterizing the location and depth of surface and near-surface defects is therefore essential for optimizing treatment processes and ensuring reliable enhancement of surface integrity and mechanical performance.

3.4 Productivity of ferrous alloys

As the industrial relevance of AM continues to expand, there is growing interest in applying PBF-LB to ferrous alloys beyond stainless steels. These materials, particularly low-alloy steels are widely used across sectors such as automotive and tooling industries due to their favourable strength-to-cost ratio and broad availability. However, while alloys like 316L have demonstrated excellent printability, more complex ferrous systems, including martensitic low-alloy steels, present unique processing challenges. This section examines the current state of productivity strategies for key ferrous alloy groups, contrasting their behaviour and limitations in the context of PBF-LB, and highlighting the trade-offs between build rate and material integrity.

3.4.1 Low alloy steel

Low-alloy steels are iron-based alloys characterized by carbon contents up to approximately 0.60 wt.% and less than 10 wt.% total alloying additions, typically including elements such as chromium (Cr), molybdenum (Mo), and manganese (Mn) [78]. These steels are widely used in structural applications where high strength, good toughness, and cost-effectiveness are required [79]. Their relevance spans multiple industries, including automotive, tooling, and energy, where they are commonly employed in pressure systems, drilling tools, and high-strength piping. The potential to leverage these properties in PBF-LB is significant, particularly for producing spare parts on demand. In conventional supply chains, spare parts often require substantial warehousing and upfront capital, with many components never used. PBF-LB offers an alternative path by enabling on-demand, sustainable [8] and distributed manufacturing [31]. However, realizing this potential requires overcoming substantial challenges in processability and productivity due to the complex thermal behaviour of these alloys.

These challenges arise primarily from the martensitic phase transformation that occurs during rapid cooling. While the solidification phase typically produces austenite, the extremely high cooling rates inherent to PBF-LB suppress diffusional transformations and instead trigger a solid-state transformation to martensite. The resulting microstructure, often dominated by brittle martensite, can contribute to high mechanical strength, but also increases brittleness and residual stress. The risk of cold cracking is specifically high in alloys with greater carbon content. Operating at higher VED can lead to increased cyclic reheating due to larger melt pool dimensions, as a greater volume of material is reheated. The increased reheating effect may lead to reduced cooling rates, which can subsequently decrease the likelihood of cold cracking [80]. Additionally, many PBF-LB systems include build plate preheating capabilities, which assist in reducing thermal gradients and cooling rates, thereby helping to mitigate the risk of cold cracking during fabrication [81]. Figure 11 illustrates a typical Nital-etched cross-section of a 4130 low alloy steel specimen fabricated via PBF-LB. The overall microstructure consists of tempered martensite due to the cyclic reheating, while Fig. 11b reveals a brighter region near the top surface, typical for untempered martensite formed during cooling of the final layer.

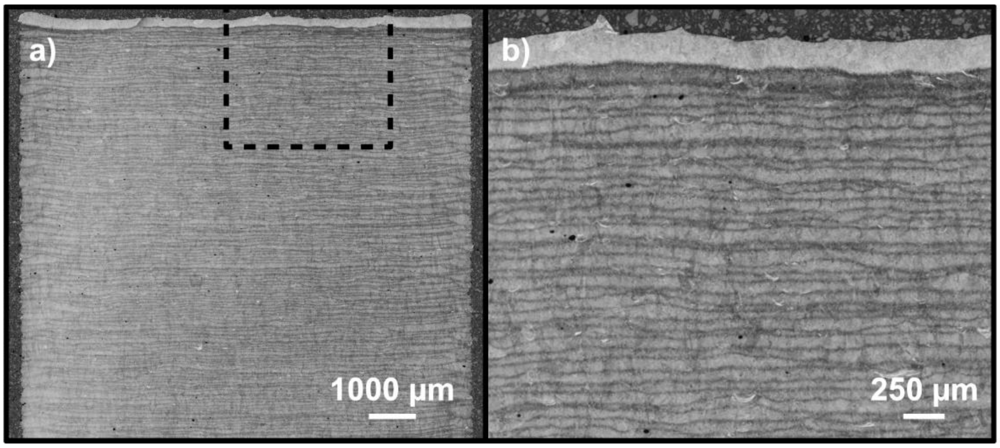

Figure 11: Micrograph illustrating the Nital-etched microstructure of 4130 low alloy steel fabricated via PBF-LB. The image on right highlights the untempered martensite present at the top layer.

To date, most studies have focused on achieving high density and crack-free structures using conservative processing conditions, typically limited to layer thicknesses of 20 to 40 µm [82]. Examples of studied low alloy steels include AISI 4130 [81,83–87], AISI 4140 [27,81,84,88,89], and AISI 4340 [81,84,90,91]. These efforts have shown that relative densities exceeding 99.8% and mechanical properties comparable to wrought counterparts can be attained when energy input, scan strategy, and preheating are optimized [92]. However, such approaches often come at the expense of productivity, limiting the feasibility of these materials for widespread adoption in serial manufacturing. To advance industrial viability, current research must now address how increased build rates, through thicker layers and higher scan speeds, affect the development of microstructure, in-situ tempering, and defect formation. Understanding these relationships is important to unlocking the use of low-alloy steels in cost-effective, high-throughput additive manufacturing workflows.

3.4.2 316L stainless steel

In contrast, 316L stainless steel is one of the most established and well characterized alloys for PBF-LB. It is an austenitic stainless steel with a low carbon content (typically below 0.03 wt.%), which prevents carbide precipitation and intergranular corrosion. Its structure is stabilized by Nickel (Ni) and Mo additions, allowing it to retain a fully austenitic phase during cooling and avoid martensitic transformation [93]. This contributes to high process stability during PBF-LB and makes 316L suitable for applications in industries with stringent material requirements, such as medical, energy, and food processing [1].

The microstructure of PBF-LB 316L is hierarchical and highly refined. It consists of overlapping melt pools (Fig. 12a), columnar grains aligned along the build direction, and sub-micron solidification cells (Fig. 12b). At higher magnification, nanoscale cells are visible, the boundaries of which are enriched in elements such as chromium and molybdenum (Fig. 12c). These solute-enriched boundaries hinder dislocation motion and enhance mechanical strength [54].

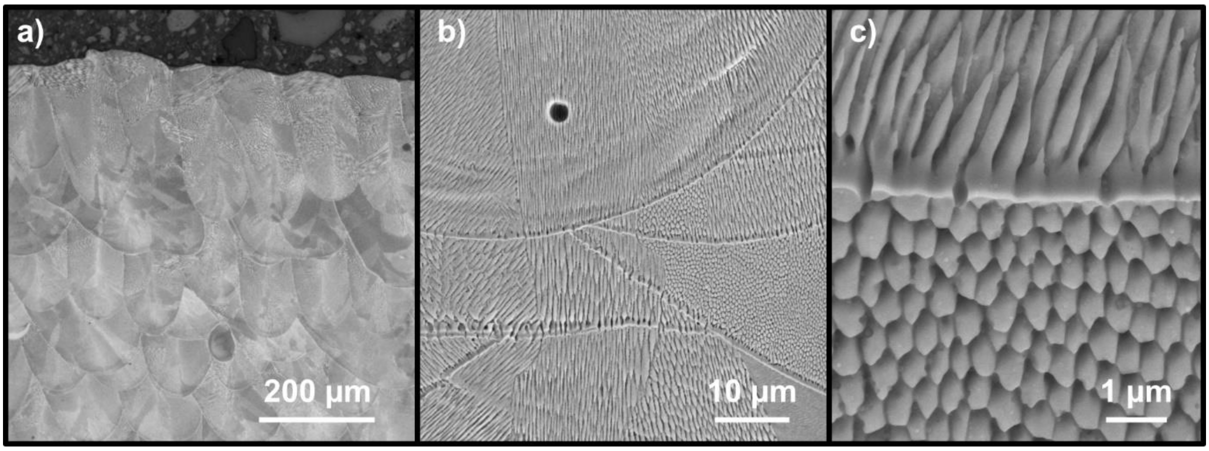

Figure 12: Hierarchical microstructure of PBF-LB stainless steel 316L revealed by oxalic acid a) optical micrograph of overlapping melt pools, b) SEM micrograph of grain and cell structure and c) sub-micron cell structure at a melt pool boundary.

Due to its favourable processability and defect tolerance, 316L has become the reference alloy in PBF-LB research [94]. Numerous investigations have explored methods for increasing production speed, frequently achieved by employing greater layer thicknesses [95]. Tensile properties are generally within specification and often superior to conventionally processed counterparts due to the fine cellular microstructure. Reported properties include yield strengths of approximately 540 MPa and elongations exceeding 60% at 20 µm layer thickness. At higher layer thicknesses, such as 80 µm, yield strength tends to drop to around 465 MPa, and elongation is typically reduced to ~44%, but still within acceptable limits for wrought 316L [96]. These reductions are attributed to increase in LoF porosity.

Fatigue behaviour at high build rates remains one of the key limitations to the widespread adoption of PBF-LB 316L stainless steel in load-bearing applications. Although this alloy offers excellent ductility and high yield strength in the as-built condition, its fatigue performance is significantly influenced by high surface roughness and internal defects formed during fabrication [97]. These include surface roughness and LoF pores, both of which serve as crack initiation sites under cyclic loading, particularly in high-cycle fatigue (HCF) conditions.

Once surface roughness is minimized, internal porosity becomes the dominant fatigue-limiting factor. The size, shape, and orientation of pores can have a greater influence on crack initiation than pore fraction alone [12]. For example, LoF defects aligned perpendicular to the loading direction are significantly more detrimental than those aligned parallel for static properties. Impact of the defect size and distribution on fatigue properties is not well understood. Although static mechanical properties of 316L remain within specification even at increased build rates, changes in pore morphology are not as well documented. This highlights the need for a deeper understanding of how high-productivity processing strategies affect the formation of fatigue-relevant defects and their interaction with applied stresses. And how the pore characteristics of pores vary with different process parameters such as hatch distance and scan speed extending beyond only layer thickness.

Currently, original equipment manufacturers (OEM) recommend process parameters, such as those provided by EOS for the M290 platform, illustrating the state of the art in balancing productivity and part quality. For 316L, standard settings achieve approximately 99.9% density at a build rate of ~13 cm³/h using 40 µm layer thickness, and around 99.8% density at ~30 cm³/h with 80 µm layers [98]. These parameters provide a reliable and validated baseline for industrial use and serve as the reference point for this thesis. However, to further advance the productivity of PBF-LB, especially for application critical components, it is essential to explore how deviations from these baseline parameters affect defect formation, surface integrity, and fatigue performance. The following chapters aim to quantify these effects, assess the implications for post-processing requirements, and ultimately define strategies for achieving high build rates without compromising mechanical integrity.

4. Materials and Methods

This section provides a summary of the materials and analytical techniques used in this research. For detailed descriptions of the materials and experimental setups the reader is referred to the appended papers.

4.1 Materials and PBF-LB system

The metal powders used in this study were produced via gas atomization, resulting in a predominantly spherical morphology and particle size distributions of between 20 and 64 µm. All powders used were virgin, with no recycling or reuse between builds, ensuring consistency in material input. Most of the powders were supplied by Höganäs AB (Sweden), including two low-alloy steels and 316L stainless steel, as detailed in Table 3. In the final study (**Paper VI**), a 316L stainless steel powder was sourced from EOS GmbH (Germany), also listed in Table 3.

Table 3: Chemical composition (wt. %) of studied ferrous alloys

	C	Cr	Mo	Ni	Mn	Si	O	Fe	Supplier
AISI 4130	0.34	1.0	0.20	-	0.60	0.30	0.05	Balance	Höganäs AB
AISI 4140	0.47	1.0	0.20	-	0.60	0.20	0.07	Balance	Höganäs AB
AISI 316L	0.03	16.9	2.50	12.60	1.50	0.70	0.06	Balance	Höganäs AB
AISI 316L	0.02	17.1	2.73	13.40	1.42	0.38	-	Balance	EOS GmbH

All specimens in this thesis were manufactured using an EOS M290 machine equipped with a 400 W ytterbium fibre laser (spot size: ~85 µm, Gaussian intensity profile). A high-purity argon atmosphere with constant flow was maintained throughout all builds, keeping oxygen levels at below 1000 ppm. Consistent processing conditions were applied in all studies, except for the low-alloy steel builds, where the build plate was preheated to 180 °C. In comparison, a preheat temperature of 80 °C was used for the 316L stainless steel builds.

The sample geometries varied depending on the research focus of each study. For instance, studies primarily focused on process mapping (**Paper I** and **Paper III)** utilized simple 10x10x10 mm^3 cubes. The geometries used for all builds are presented in Figure 13.

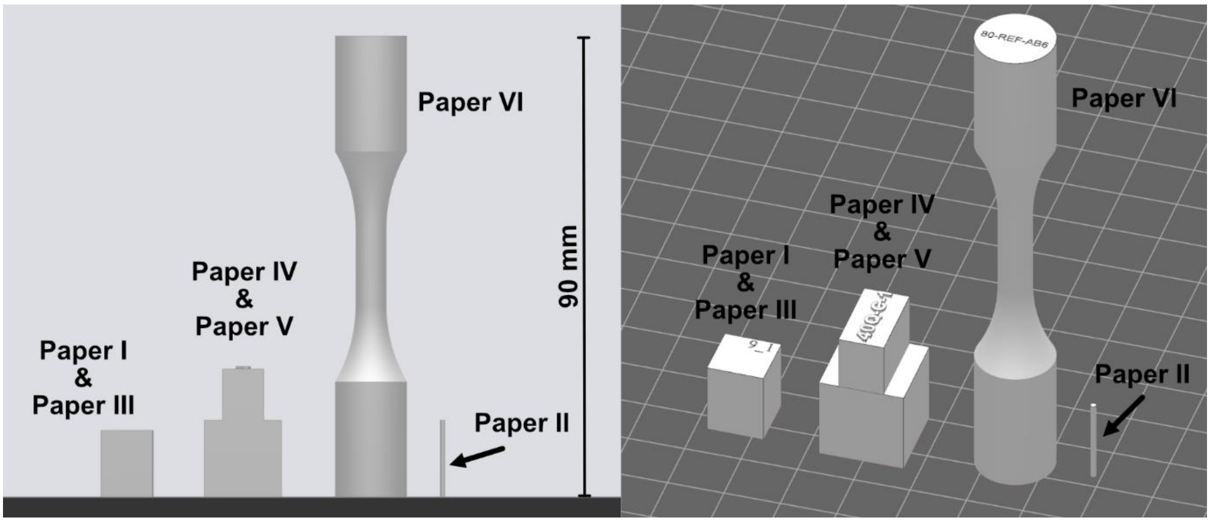

Figure 13: 3D geometries studied in this work as seen in EOSprint2.8 software.

4.2 Process parameters for increased build rates

With the aim of achieving increased build rates, initial process mapping was performed across the four layer thicknesses 20, 40, 60 and 80 µm (**Paper I**). For 316L stainless steel, the standard parameters provided under material licenses (316L_Surface_1.X and 316L_040_FlexM291_1.X from EOS GmbH, Germany) were used as a baseline for the 20 and 40 µm layer thicknesses. Based on these, a design of experiment was developed to explore increased build rates by varying laser power (195 – 280 W), hatch distance (90 – 270 µm), and scan speed (600 – 1800 mm/s). For the 60 and 80 µm layer thicknesses, where material licenses were unavailable, new process parameters were established using the work of Leicht et al. [99] as a foundation. **Paper I** contain more information about the design of experiments strategy. Subsequent studies on 316L stainless steel (**Papers II** and **IV-VI**) then either employed standard parameters at 40 µm (**Papers IV** and **V**) or utilized specific parameters selected from the process mapping in **Paper I**.

For the low alloy steel (**Paper III**), the parameters investigated were based on the foundational work of Hearn et al. [92], who conducted detailed process mapping for various low alloy steels at a 20 µm layer thickness. Given the relatively less extensive research on low alloy steels within the PBF-LB community, some parameters were kept constant while the impact of build rate on processability was studied by varying layer thickness (20, 40, and 60 µm), scan speed (640 – 1490 mm/s), and laser power (170 – 250 W), with a constant hatch distance of 70 µm.

4.3 Surface treatments

A targeted material removal of approximately 110 µm per surface was employed for post-processing of PBF-LB 316L specimens using two different techniques, both aimed at eliminating surface features inherent to the PBF-LB process, such as adhered powder and melt pool tracks, to reduce surface roughness.

The processing differed between the two methods: Chemical Mechanical Processing (CMP), performed by REM Surface Engineering, USA [75] combined mechanical abrasion with a material-specific chemical compound within a vibratory bowl containing non-abrasive ceramic media, where a chemically formed, easily removed layer was preferentially removed by the mechanical action over approximately six hours, culminating in a smoother, mirror-like finish with rounded edges. In contrast, Hirtisation®, conducted by RENA Technologies GmbH, Austria [99], utilized a combination of chemical and electrochemical processes specifically tailored to the alloy system.

4.4 Metallography

Samples were removed from the build plate via electric discharge machining (EDM) to prepare them for microstructural characterization. Each sample was then sectioned along the BD-X plane (Figure 14) using a Buehler Isomet 2000 precision saw and mounted in Polyfast resin. Grinding followed with SiC foil (320-2000 grit) on a Struers TegraPol, and fine polishing used 3 µm and 1 µm diamond suspension for a mirror finish. As-polished samples were used for pore fraction measurements, pore characteristics, and hardness tests in **Paper III**.

Microstructure and melt pool boundaries were revealed using specific etchants: 3% Nital solution for martensitic low alloy steels and electrochemical etching in 10% oxalic acid (3V, platinum cathode) for austenitic 316L. Melt pool width and depth (µm) were estimated and averaged across 30 melt pools on the top surface of each sample in both studies in **Paper I** and **Paper III**.

4.5 Characterization techniques

4.5.1 Light optical microscopy (LOM)

A Zeiss Axiovision 7 light optical microscope (LOM) at ×5 magnification (0.88 µm × 0.88 µm per pixel) captured micrographs of as polished and etched samples. The proprietary software stitched sequentially acquired images to create large montages covering a 5 × 5 mm² area. These 8-bit grayscale images (0-255 grey values) were analysed using the Matlab image processing toolbox. In **Paper II**, pore fraction levels were calculated on binary images using a grey value threshold of 170. Stitched micrographs were cropped to isolate the bulk material. Pore shape descriptors (orientation, major/minor axis length, aspect ratio) were calculated using the *regionprops* function in Matlab (part of the Image Processing Toolbox), with correlations to sample cross-sections illustrated in Figure 14. **Paper III** utilized ImageJ (Fiji) software for low alloy steel analysis, following established guidelines [100].

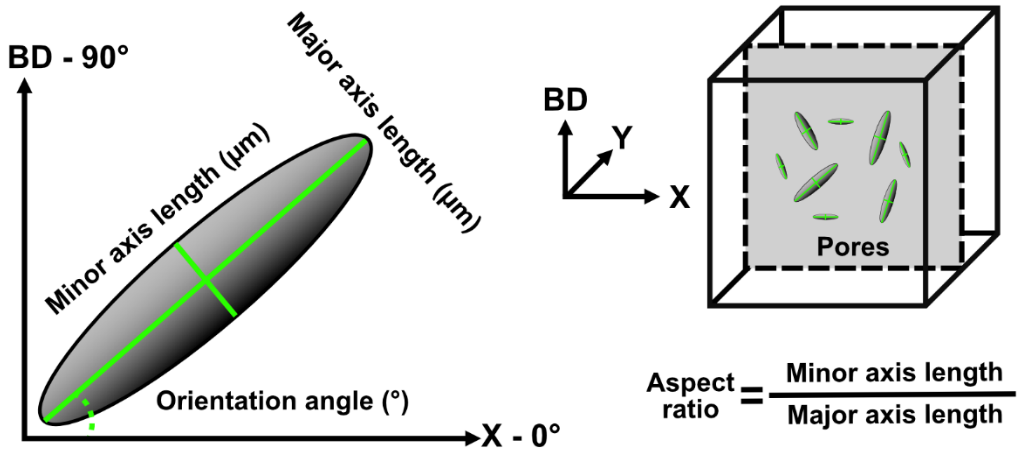

Figure 14: Pore characteristics of interest in **Paper I** [101].

4.5.2 Scanning electron microscopy (SEM)

Scanning electron microscopy (SEM) using a Zeiss Gemini 450 FEGSEM provided topography and feature analysis of as-built outer surfaces and microstructure characterization of polished cross-sections via secondary electrons (SE). Surface topography imaging used lower acceleration voltages (10 kV) compared to the 20 kV employed for high-resolution imaging of polished cross-sections. Electron backscatter diffraction (EBSD) was also utilized with an Oxford Instruments Symmetry CMOS detector attached to the Gemini 450. By tilting crystalline samples at 70°, diffracted backscattered electrons (originating 10-50 nm from the surface) formed Kikuchi bands. Analysis of these bands revealed crystal lattice information at each measurement point, enabling the creation of detailed maps showing phase distribution, grain size, texture, and local deformation [102]. Large area EBSD mapping of as-built and CMP-processed microstructures was performed in **Paper V** on the Zeiss Gemini 450 at 20 kV with a 1.5 µm step size. Higher magnification EBSD for Kernel Average Misorientation (KAM) maps used a 0.2 µm step size and a maximum misorientation angle of 2° to exclude grain boundary effects. All EBSD data were processed using AztecCrystal3.3.

4.5.3 X-ray computed tomography (XCT)

X-ray computed tomography (XCT) is a non-destructive testing method used to analyse the internal porosity of materials. For detailed pore characterization in **Paper II**, synchrotron X-ray computed tomography (SXCT) was employed at the BAMline, BESSY II in Berlin [103], achieving a high resolution with a 0.72 µm voxel size. However, the SXCT limitation on sample size meant only 1 mm diameter cylinder specimens could be investigated at this resolution. In **Paper VI** XCT scans on fatigue bars were conducted using a laboratory CT scanner, a GE v|tome|x 300 L, with settings of 200 kV and 40 µA applied to the X-ray tube. The reconstructed voxel size was 8 µm, and only the gauge region (6 mm diameter) of the samples was measured. Pores smaller than 30 µm were excluded to minimize noise, and Avizo software was used for porosity segmentation and analysis.

4.5.4 X-ray diffraction (XRD)

X-ray diffraction (XRD) is a highly effective technique for analysing strain, residual stress, and phase composition in crystalline materials. The fundamental principle of XRD is Bragg´s law, which relates the wavelength of incoming X-rays (λ), the interplanar spacing (d) and the diffraction angle (θ), where changes in interplanar spacing d reflects changes in elastic strain (d_0 strain free state). Several destructive and non-destructive techniques are available to determine the residual stresses within a material. Due to their non-destructive nature, diffraction methods are, naturally, the most widespread for the characterization of residual stress.

Within the scope of this work synchrotron X-ray diffraction (SXRD) measurements were performed at the white beam engineering materials science beamline P61A at the Deutsches Elektronen-Synchrotron (DESY) in Hamburg, Germany [104]. These measurements were performed to study the subsurface residual stress state of PBF-LB/316L produced cubes before and after post processing by Hirtisation and CMP.

4.5.5 Surface topography

Surface topography analysis was performed in **Paper IV-VI** to quantify the surface roughness of as-built PBF-LB/316L and after being subjected to Hirtisation and CMP post processing. These measurements were performed in an optical profilometer SensoFar Neox S instrument combined with confocal fusion. Stitching of a 3.2 x 2.4 mm^2 areas in the BD-Y plane parallel to the build direction for cubes and on 0.65 x 5.34 mm^2 areas along the gauge section for as-built fatigue bars. Surface plots and roughness measurements were processed and extracted in Mountains Map 10.1 [105]. Main surface texture parameters of interest were (S_a, S_{10z}) in accordance with the ISO 25178-2 standard [106].

4.5.6 Mechanical testing

In **Paper III**, a DuraScan 70-G5 device was utilized to carry out 16 Vickers microhardness (HV10) indentations arranged in a 4 × 4 grid, with 2.5 mm spacing between each point, on every sample. This setup aimed to assess the effect of process parameters on hardness and was conducted following the ASTM E384 – 17 standards [107].

The fatigue tests covered in **Paper VI** were performed at Linköping University on 90 mm height cylindrical bars with an as-built 6 mm gauge diameter using the Instron WaveMatrix system, which had a dynamic load capacity of ±50 kN and operated at a frequency of 5 Hz. Throughout the tests, a stress ratio ($R = \sigma_{min}/\sigma_{max}$) of -1 was applied. All the fatigue test series were performed within the stress ranges of 175 MPa and 550 MPa. The applied forces were adjusted to be consistent with the reduced cross-sectional area due to post-treatments. All fractographic analyses were performed using a JEOL JSM-IT500 SEM. The examination focused on the bottom half of the specimens, specifically selecting those samples that failed under fatigue testing at a stress range of 350 and 450 MPa.

5. Results and Discussion

Paper I – III and **Paper VI** study pore characteristics of porosity generated at increased build rates. In **Paper I**, the connection between process parameters and porosity was investigated across a wide range of layer thicknesses, hatch distances and scan speeds. The influence of each parameter at an increased build rate was captured. In **Paper II** the pore characteristics of selected conditions were further analysed by synchrotron X-ray computed tomography enabling high resolution 3D reconstructions of pores at increased build rates. **Paper III** examined the connection between increased build rates and cold cracking of low alloys steels.

Paper IV and **V** investigated post-AM surface treatments to reduce surface roughness of as-built components. In **Paper IV** the influence of as-built surface topography and microstructures on surface material removal by the electrochemical Hirtisation® process is analysed. Recommendations for achieving uniform material removal by tailoring the scan strategy were provided. Similar analysis was performed in **Paper V** but using the chemical mechanical polishing (CMP) process. Being a combination of chemical and abrasive process, the work addresses the changes in surface and subsurface residual stresses by XRD measurements.

Paper VI connects the detailed characterization performed in **Paper I-V**, pore characteristics and surface treatments to fatigue properties at increased build rates.

5.1 Impact of build rate on pore characteristics and fatigue properties

5.1.1 Process mapping

Extensive process mapping was conducted on PBF-LB/316L cubes to investigate the impact of key printing parameters on porosity levels (%). The primary objective was to understand how pore fraction varied at different layer thicknesses (20, 40, 60, and 80 µm) as a function of laser power, scan speed, and hatch distance. This approach was chosen because layer thickness has the largest influence on the build rate. Process windows were defined based on pore fraction (%) measurements obtained from image analysis of optical micrographs of polished cross-sections. This section will present these process maps using combined parameters and compare them with response surfaces generated through linear regression.

Combined parameters vs pore fraction

Figure 15 demonstrates the applicability of the combined parameter VED and its relationship with measured porosity over a wide range of processing conditions for 316L stainless steel. Porosity tends to decrease with increasing VED across the entire investigated process region. Nonetheless, notable differences in porosity, reaching up to 7.5%, were observed even at identical VED values. The selected micrographs in Figure 15 highlight that these differences are due to the use of larger hatch distances rather than variations in scan speed. Consequently, the effectiveness of VED as a sole indicator of porosity is limited when a wide range of process parameters is employed as previously shown by [30]. However, as shown in **Paper 3**, maintaining a constant hatch distance reveals more predictable trends in terms of VED and SED (Figure 16).

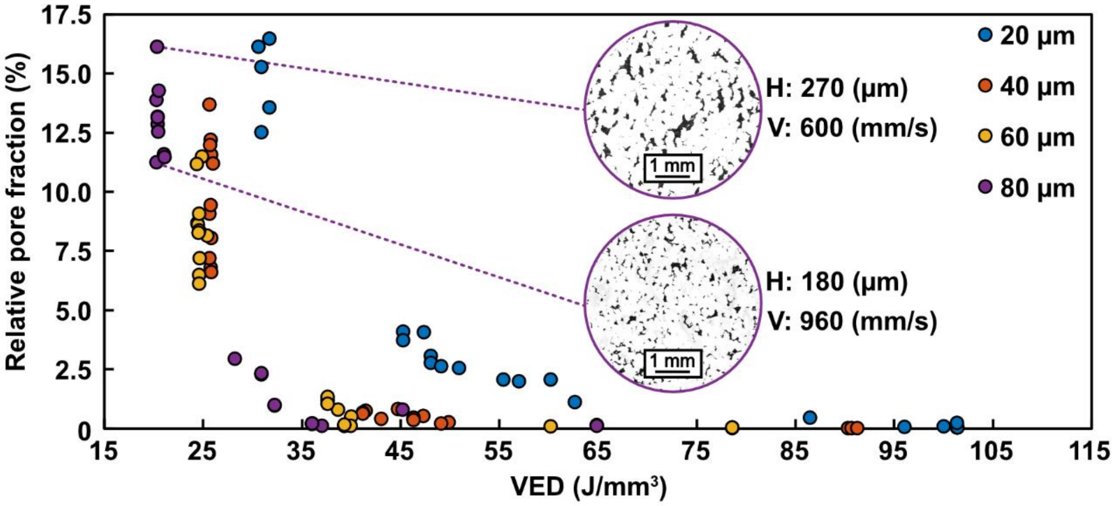

Figure 15: Influence of the combined process parameter VED J/mm^3 on pore fraction at 20, 40, 60 and 80 µm layer thickness.

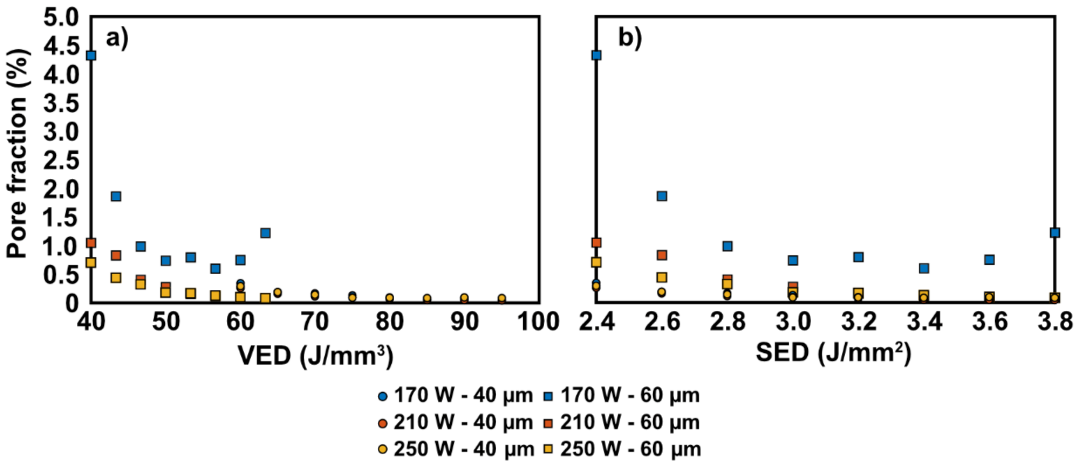

Figure 16: Influence of the combined process parameters a) VED J/mm^3 and b) SED J/mm^2 on pore fraction at 40 µm and 60 µm layer thickness of low alloy steels.

Regression modelling of pore fraction

Given the weak correlation observed between VED and porosity in the experiments of **Paper I**, predictive modelling via linear regression was employed as an alternative. The relative pore fraction was modelled as a function of laser power, scan speed, and hatch distance, with separate models developed for each layer thickness (20, 40, 60, and 80 µm). The results of these regression models are visualized in Figure 17 as contour plots, illustrating the interplay between hatch distance (x-axis) and scan speed (y-axis) on the predicted relative pore fraction at a laser power of 280 W for each layer thickness.

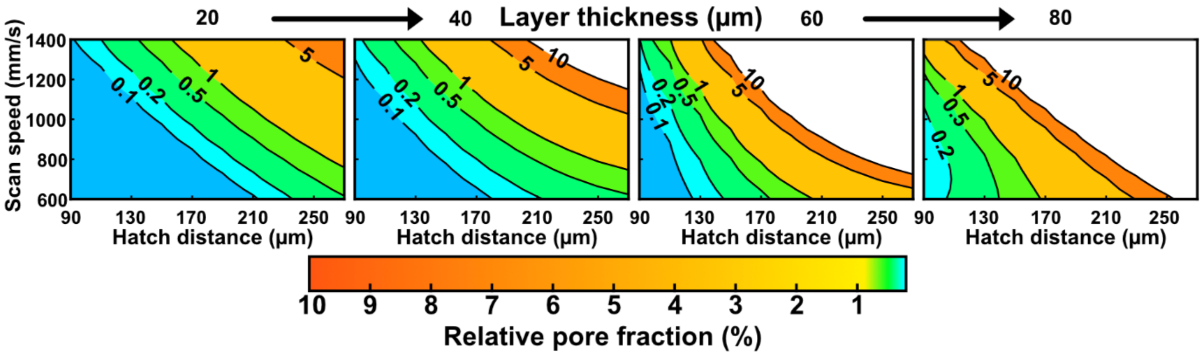

Figure 17: Contour surfaces illustrating the interaction between scan speed and hatch distance at 20, 40, 60 and 80 µm layer thickness on pore fraction separately at 280 W laser power.

The contour plots in Figure 17 reveal a clear trend where the processing parameter space predicting very low relative pore fractions reduces as the layer thickness increases from 20 to 80 µm. For the 80 µm layer thickness, this optimal processing region for achieving minimal porosity becomes restricted to the corner of low scan speeds and small hatch distances. This four-fold increase in layer thickness leads to a significant reduction in the processing space predicted to yield low porosity, consistent with prior research [99], which is a consequence of the corresponding four-fold decrease in remelting cycles.

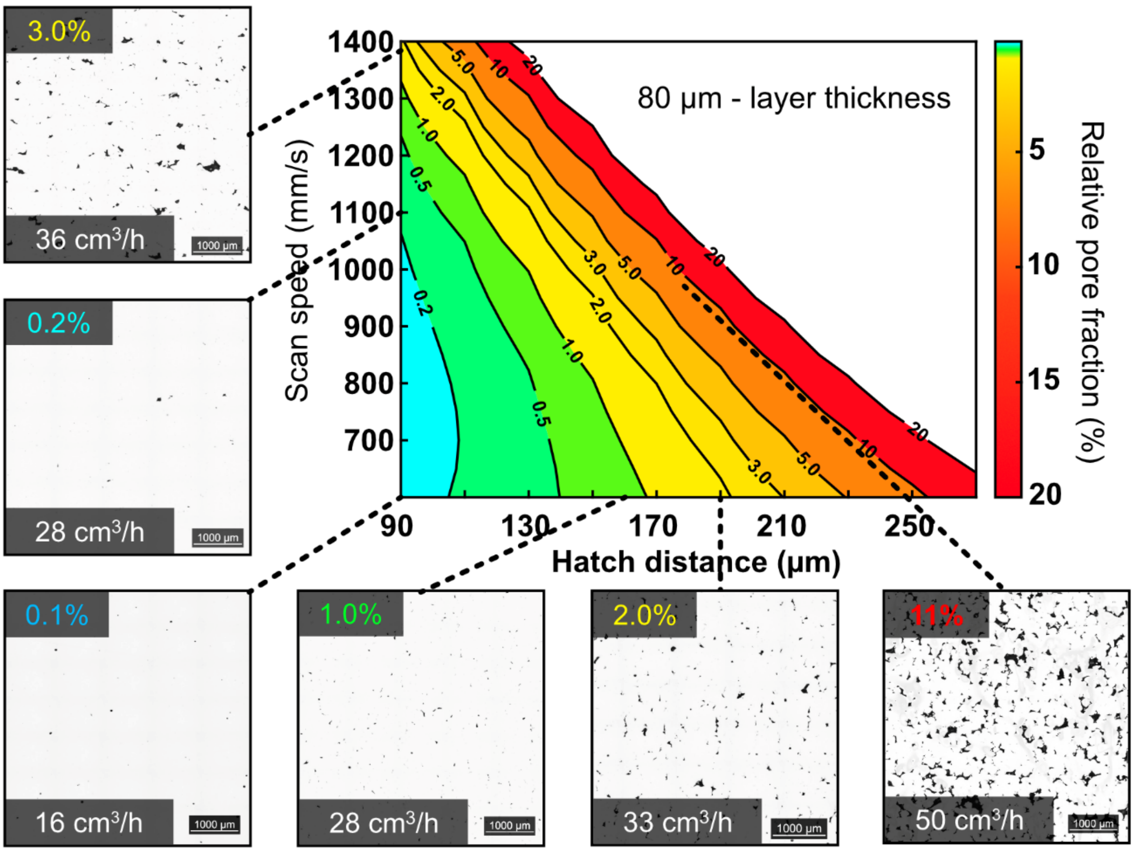

Figure 18: Influence of scan speed and hatch distance on pore fraction (%) at increased build rates adapted from [108].

The regression models were validated by comparing the predicted porosity contours with experimental measurements. The predicted relative pore fraction in Figure 18 illustrates how porosity evolves with increasing build rate in these two dimensions for an 80 μm layer thickness. The figure also presents representative micrographs displaying the pore characteristics at various build rates and highlights the correspondence between the model predictions and actual porosity measurements. The close agreement between the contour surface and the experimental data suggests a good accuracy of the regression model. This agreement indicates that regression modelling offers a more reliable approach for parameter selection compared to the VED plots shown in Fig. 15.

Regarding the build rate, starting from the reference condition (Fig. 18) measuring 0.1% relative pore fraction at a build rate of 16 cm^3/h, increasing the build rate along either the hatch distance or scan speed axis leads to an increase in the obtained pore fraction by introducing sharp elongated LoF pores. At a ~80% increase in build rate to 28 cm^3/h, increasing scan speed resulted in a lower pore fraction of 0.2% compared to increasing hatch distance, which yielded a pore fraction of 1.0%. Furthermore, at a ~120% increase in build rate from the near-fully dense condition, the conditions achieved by increased hatch distance and increased scan speed show similar porosity levels and build rates but distinct pore characteristics. As the orientation of pores is known to influence mechanical properties [63,64,109], a detailed description of these processing conditions is crucial.

5.1.2 Impact of build rate on pore characteristics

2D image analysis

Having established the relationship between build rate and pore fraction, the subsequent analysis focused on characterizing how the pore characteristics, namely size, shape, and orientation, varied under different high build rate conditions. Quantification of selected conditions through 2D image analysis in **Paper I** revealed clear differences in pore characteristics between high build rates achieved by increasing hatch distance (Figure 19a) and increasing scan speed (Figure 19b). For pores larger than 100 μm, the average orientation angle was 70°, in the case of increased hatch distance, indicating an alignment close to the build direction. In comparison, higher scan speeds resulted in an orientation angle of 25°, indicating that pores were more aligned perpendicular to the build direction. Choo et al., [63] showed that pores oriented perpendicular to the loading axis result in reduced yield strength and ductility compared to pores aligned along the loading direction. Thus, the method of increasing the build rate significantly affects the anisotropy of mechanical properties. Therefore, the choice of parameters for increasing the build rate should carefully consider the load case in the final application.

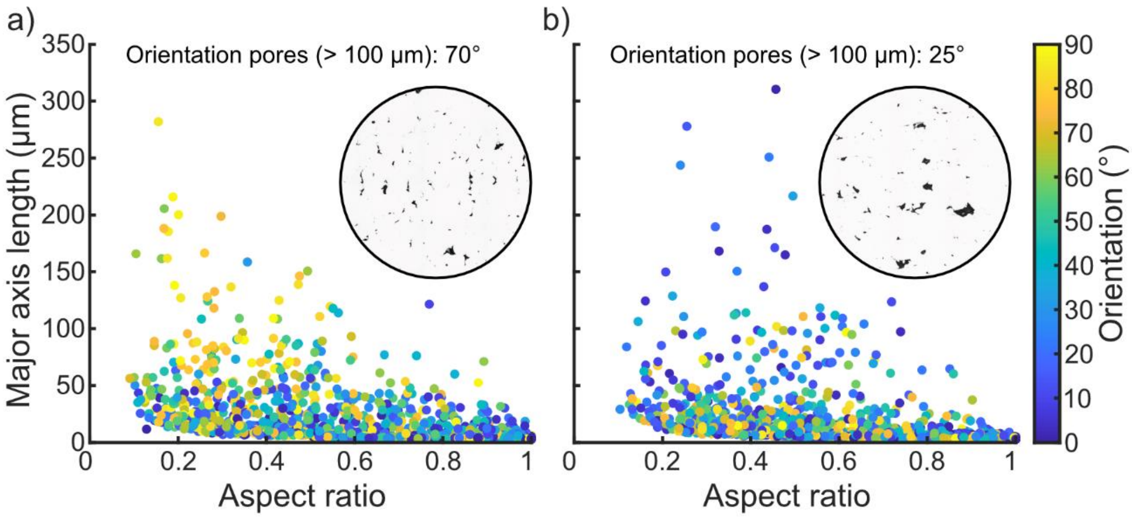

Figure 19: Influence of a) hatch distance and b) scan speed on pore characteristics namely, size, aspect ratio and pore orientation adapted from [101].

3D reconstructions by SXCT influence of layer thickness and hatch distance

The pore characterization in **Paper I** was based solely on 2D image analysis, potentially leading to a misinterpretation of the spatial distribution of pores, selected conditions from the process maps in **Paper I** were further analysed using SXCT at the BAMline, BESSY II in Berlin. This technique enabled high-resolution 3D reconstruction of the pores with a voxel size of 0.72 µm. Two 1 mm diameter cylinders were fabricated at each layer thickness, representing minimized pore fraction (Q) and increased productivity (P) (achieved with larger hatch spacing), and then analysed using SXCT.

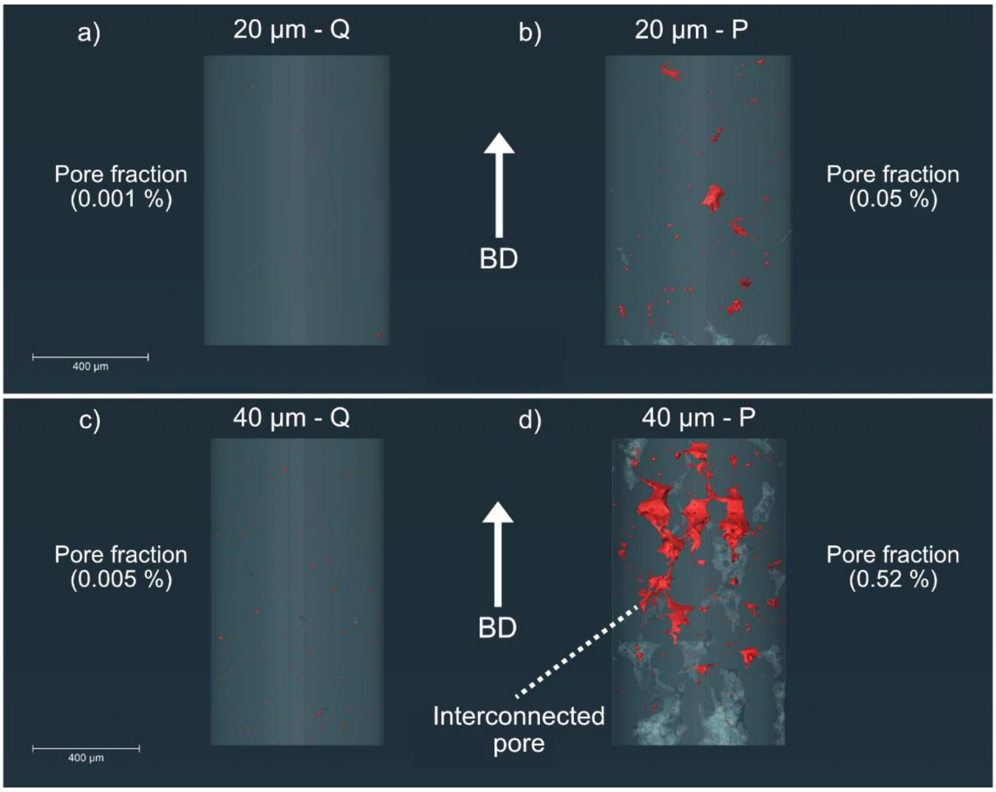

Figure 20: 3D reconstruction of SXCT data illustrating pores present a) - b) 20 µm layer thickness and c) - d) 40 µm layer thickness and the influence of 2.5 factor increase in hatch distance corresponding to 250 µm adapted from [110].

A key contribution of the SXCT measurements in **Paper II** was the high-resolution 3D capture of pore distribution at increased build rates for both Q and P conditions, revealing details missed by 2D analysis. The 3D reconstructions for 20 µm and 40 µm layer thicknesses are presented in Figure 20. For the Q conditions (Fig. 20a and 20c), predominantly spherical pores with low pore fractions (0.001% and 0.005% for 20 µm and 40 µm, respectively) were observed, with the 40 µm - Q sample showing slightly larger pores. Increasing the hatch distance to 250 µm in the P conditions resulted in higher pore fractions (0.05% for 20 µm - P and 0.52% for 40 µm - P). The 20 µm - P sample (Fig. 20b) contained a few large pores (up to 140 µm) with a slight deviation from the build direction. Notably, at a 40 µm layer thickness under P conditions (Fig. 20d), a large pore (maximum size of 540 µm) interconnected between layers with a slight angle was observed, oriented parallel to the build direction. This interconnection and slight angularity between layers made these pores impossible to fully capture using 2D optical analysis, emphasizing the importance of XCT measurements, especially at higher pore fractions.

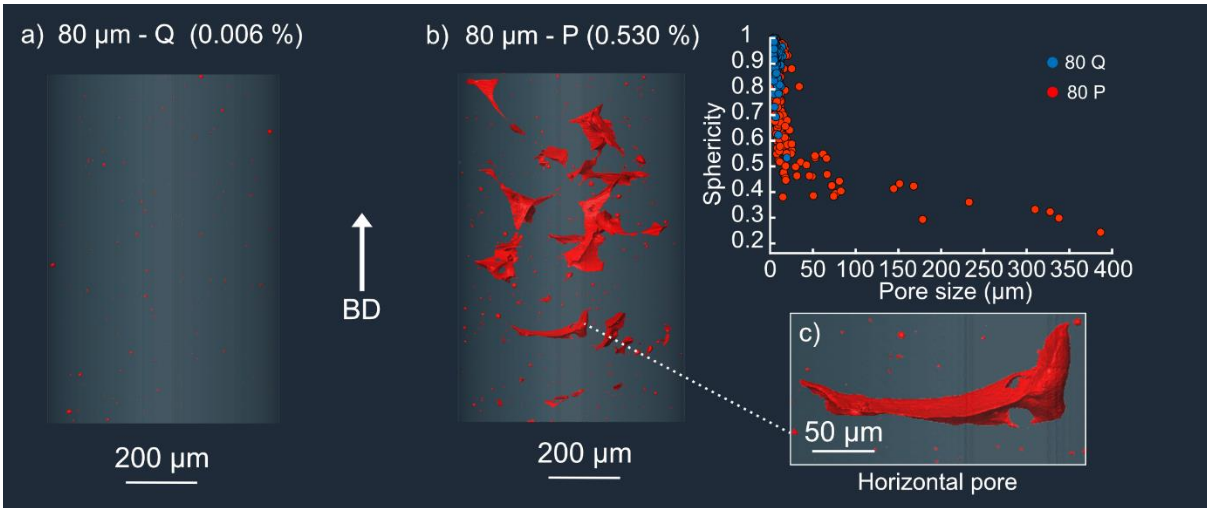

Figure 21: 3D reconstructions of SXCT data and sphericity as a function of pore size, illustrating pores present at 80 µm layer thickness a) Q condition b) P condition with a 2.1 factor increase in hatch distance corresponding to 210 µm adapted from [110]. In c) highlighted horizontal LoF not seen at other investigated conditions.

For the 80 µm Q condition (Fig. 21a), a very low pore fraction (0.006%) with predominantly spherical pores was observed, consistent with the trend of minimal porosity increase despite a significant build rate enhancement from 7.9 cm³/h (at 20 µm) to 23.0 cm³/h (at 80 µm). In contrast, the P condition at 80 µm (Fig. 21b), employing a larger hatch distance of 210 µm and achieving a build rate of 48 cm³/h, exhibited a substantially higher pore fraction (0.530%) with large, irregularly shaped pores reaching up to 400 µm, including unique horizontally oriented LoF pores (Fig. 16c) not seen at lower layer thicknesses as they were more parallel to the build direction.

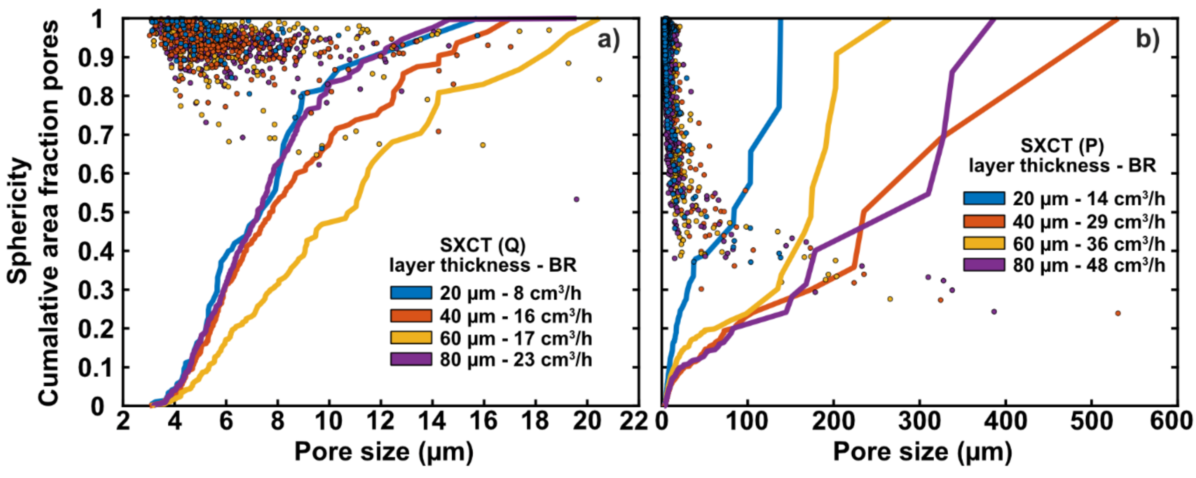

Figure 22: Sphericity (scatter) and cumulative area fraction of pores (lines) as function pore size for a) reference conditions of low porosity (Q) and b) productivity conditions (P) produced at large hatch distance. Note that the build rate of each condition is presented.

Figure 22, which provides a comprehensive summary of pore characteristics across layer thickness shows that Q conditions consistently yielded small (< 22 µm), spherical pores across the tested build rates (8 to 23 cm³/h), maintaining low pore volume fractions (0.001-0.006%). Conversely, the P conditions, achieved with larger hatch distances (250 µm for 20/40 µm and 210 µm for 60/80 µm layer thicknesses) and resulting in higher build rates (14 to 48 cm³/h), consistently showed larger (up to 540 µm), less spherical pores, leading to a substantial increase in overall porosity. The trends in Figure 22 clearly illustrate that increasing build rate by hatch distance, the formation of these detrimental larger and more irregular pores. Which is clearer at the largest build rates produced by 80 µm layer thickness.

3D pore characterization influence of scan speed and hatch distance

The SXCT results clearly showed how shape and distribution of pores changed at increased hatch distances and layer thicknesses. What was really missing was how LoF pores differed when increasing build rate through scan speed. This was further investigated in connection with fatigue properties in **Paper VI**, where laboratory XCT was performed across the gauge section prior to fatigue testing. Through the knowledge gained in **Paper I-II** it was assumed that two types of porosity could be generated at the same layer thickness while having the same build rate. Here, porosity type A (PA) was defined as LoF pores generated based on incremental increases in hatch distance (inter hatch) while porosity type B (PB) was induced by using larger scan speeds (inter layer) with respect to the reference condition representing minimal porosity. While keeping the other parameter constant at two separate porosity levels.

Figure 23 shows the changes in pore size and distribution in the gauge section in cross section (XY-plane), perpendicular to the build direction, when the build rate increases from 23 to 44 cm^3/h. The reference condition, processed at the lowest build rate of 23 cm^3/h, has a low porosity content of 0.07 %, with few visible pores that appear small and spherical, as shown in the bottom image. Using a build rate of 37 cm^3/h, the porosity content increases to 1.3 % for PA1 and 0.7 % for PB1. The pore distribution in PA1, produced at 37 cm^3/h, shows a more uniform distribution of smaller, somewhat elongated pores throughout the section, suggesting that the increased hatch distance has led to more controlled pore formation. In contrast, PB1 produced at the same build rate, exhibits fewer but larger and more irregularly shaped defects, with a less even distribution, due to the increased scan speed compared to the reference condition. At the highest build rate of 44 cm^3/h, the porosity content reaches 3.1 % for PA2 and 3.6 % for PB2. In PA2, porosity still shows a uniform distribution in a specific pattern, although size have increased compared to the lower build rate. PB2, however, displays larger, irregular and more randomly distributed defects, including open surface porosity visible in the upper right micrograph. This open porosity is particularly detrimental to fatigue life as it can act as a crack initiation site. Overall, both PA and PB exhibit increased porosity with higher build rates, but the morphology and distribution of these pores differ. PA tends to have more uniform porosity distribution, while PB exhibits larger and more irregular pores, which would lead to more detrimental defects.

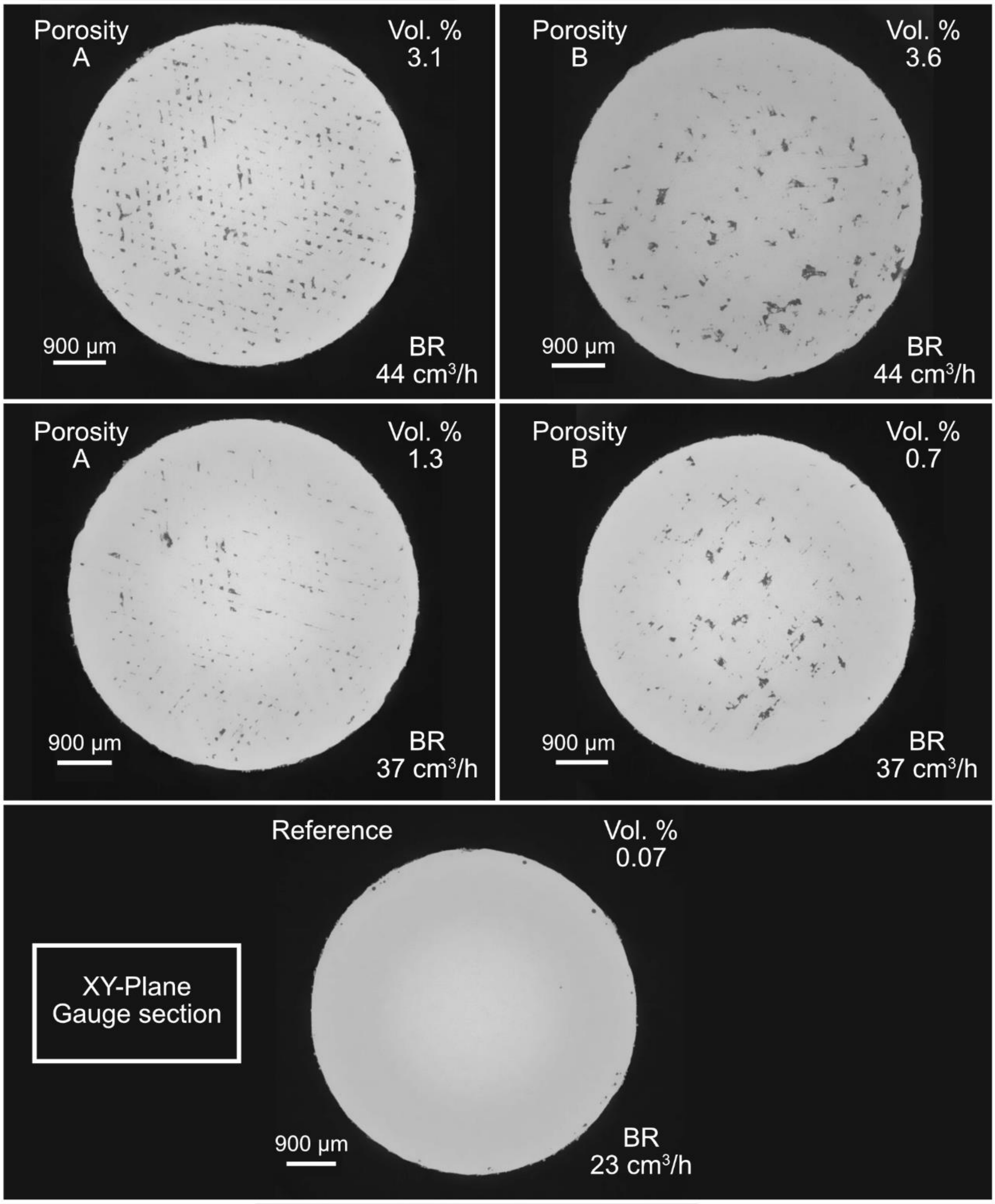

Figure 23: XCT cross-sections of the gauge region (XY-plane) showing the distribution and pore size of different as-built conditions processed at varying build rates (BR), along with the measured porosity volume fraction (Vol. %).

Figure 24a illustrates the cumulative area fraction of pores (solid lines) and the sphericity of individual pores (scattered points) for the reference (lowest build rate), PA1, and PB1 (intermediate build rate) conditions, focusing on pores with an equivalent diameter of 30 µm or greater. The equivalent diameter represents the diameter of a sphere with the same volume as the pore. As build rate increases from the reference to PA1 and PB1, the cumulative area fraction curves shift to the right, indicating that a larger proportion of the total pore area is attributed to larger pores. Alongside, the sphericity plots show a trend towards lower sphericity values for PA1 and PB1 compared to the reference condition, particularly for larger pore sizes, suggesting the formation of more irregularly shaped pores at increased build rates. For the reference, at an equivalent diameter of around 100 µm, the cumulative area fraction approaches the value of 1, signifying that almost all pore area is from relatively small spherical pores. Figure 24b presents the same analysis for the highest build rate conditions, PA2 and PB2, utilizing a different scale on the x-axis to accommodate the significantly larger pore sizes observed. Consistent with the trends in 24a, the cumulative area fraction curves for PA2 and PB2 are further shifted to the right, indicating an even greater contribution of larger pores to the total pore area. The sphericity plots for PA2 and PB2 reveal predominantly low sphericity values across a wide range of pore sizes, indicating that the larger pores formed at these high build rates are highly irregular in shape. For instance, in PB2, even at an equivalent diameter of 200 µm, the cumulative area fraction is only around 0.4, highlighting the presence of numerous large and non-spherical pores. Importantly, this analysis reveals a notable similarity in pore characteristics (pore fraction and sphericity) between the PA and PB conditions when compared at similar build rates.

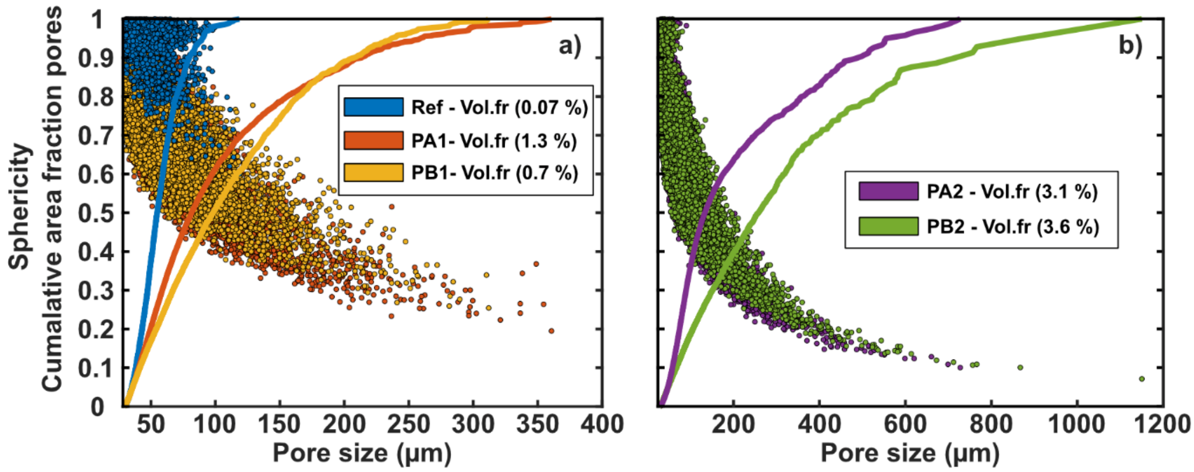

Figure 24: Sphericity (scatter) and cumulative area fraction of pores (lines) as function pore size for a) reference condition, PA1 and PB1 and b) highest level build rate for conditions PA2 and PB2. Note that the pore fraction of each condition is presented.

Analysing the orientation angles (Figure 25), it is evident that PA1 (red curve) and PA2 (purple curve) exhibit an increasingly larger fraction of pores oriented closer to the build direction (i.e., at higher orientation angles, approaching 90°) when compared to the PB conditions (yellow and green curves). It is important to note that the pores in the reference condition (blue curve) are predominantly small and spherical, as seen in the 3D reconstruction, which might lead to a less meaningful interpretation of its orientation angle trend due to the lack of a distinct major axis.

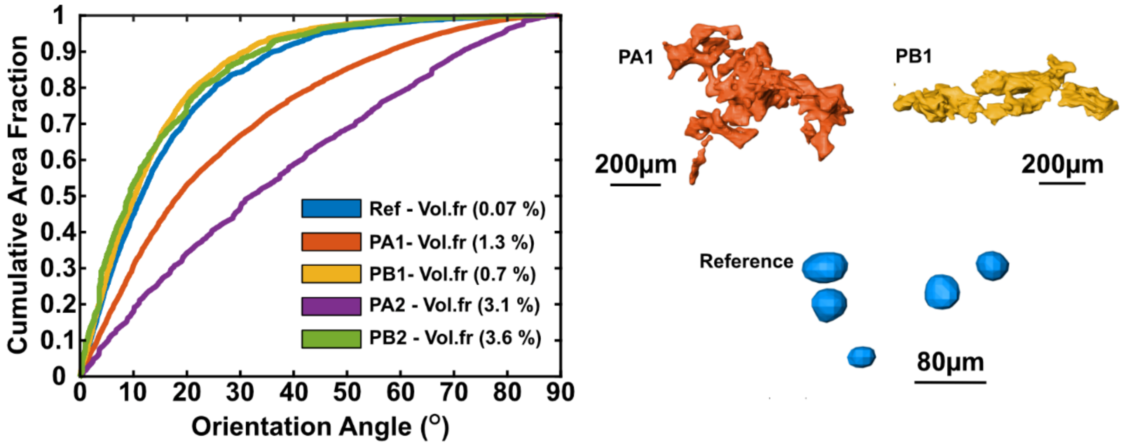

Figure 25: Cumulative area fraction of pores as a function of their orientation angle with respect to the build direction (left), and representative 3D reconstructions of the largest pores for the reference, PA1, and PB1 conditions (right).

5.1.3 Influence of pore type on fatigue life

The detailed pore characterization performed by 2D and 3D image analysis shown in previous sections provided a good understanding of the differences in pore characteristics with increased build rates. The mechanical performance was now evaluated in fatigue testing. Detailed studies of the surface topography in **Paper VI** showed that the five conditions tested could not be statistically distinguishable which illustrated that the used contour parameter provided similar surfaces evaluated by *Sa* (µm) and *S10z* (µm) 10 to 13 µm *Sa*.

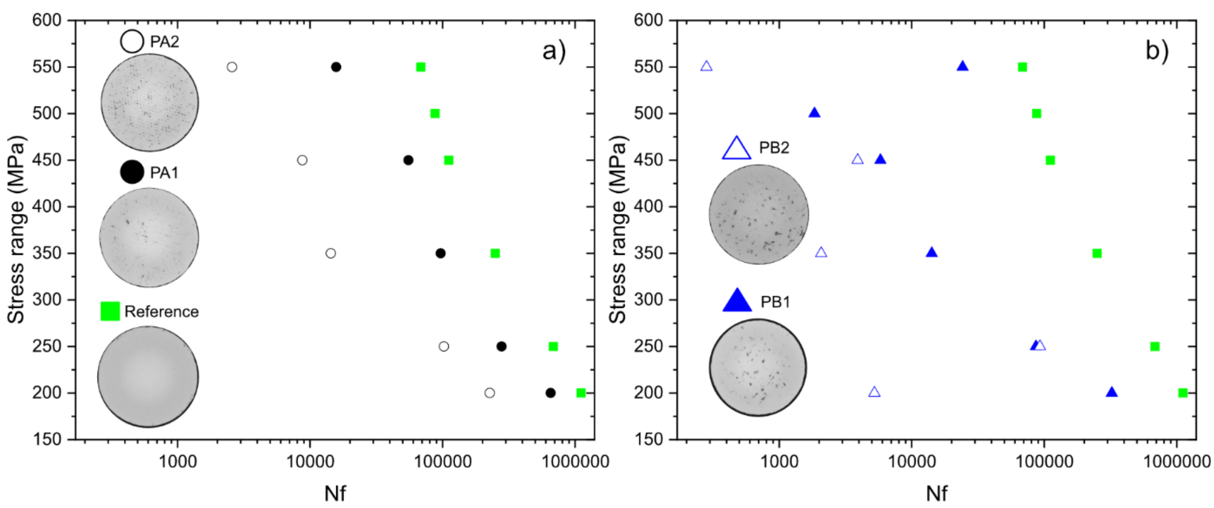

Figure 26: Influence of increased build speed and porosity type on fatigue life a) by increased hatch distance porosity type A and b) by increased scan speed (porosity type B).

In Figure 26, the reference condition, representing the lowest build rate, exhibits longer fatigue life compared to the other as-built conditions, suggesting that minimizing build rate-induced defects is beneficial for fatigue performance. By comparing porosity type A (PA1 and PA2), generated by increased hatch distance, with porosity type B (PB1 and PB2), associated with an increased scan speed, porosity type A shows longer and more consistent fatigue performance at similar build rates and stress ranges, with a trend towards reduced fatigue life observed from PA1 to PA2. The lower overall fatigue performance and increased scatter observed in porosity type B strongly correlate with the presence of more detrimental pore characteristics, larger, randomly distributed pores, and open porosity, as revealed by the XCT analysis (Fig. 23).

This was further understood by investigating the fractography (Figure 27) which compares the fracture surfaces at the largest build rate (PA1 and PA2). As seen for condition PB (Fig. 27b) the LoF pores are larger and more scattered across the fracture surface compared to the PA pores that shows a similar distribution with pores located between melt tracks. This more uniform distribution (Fig. 27a) is likely to have produced less scattered fatigue life. Higher magnification revealed more pores connected to the surface compared to the PA conditions.

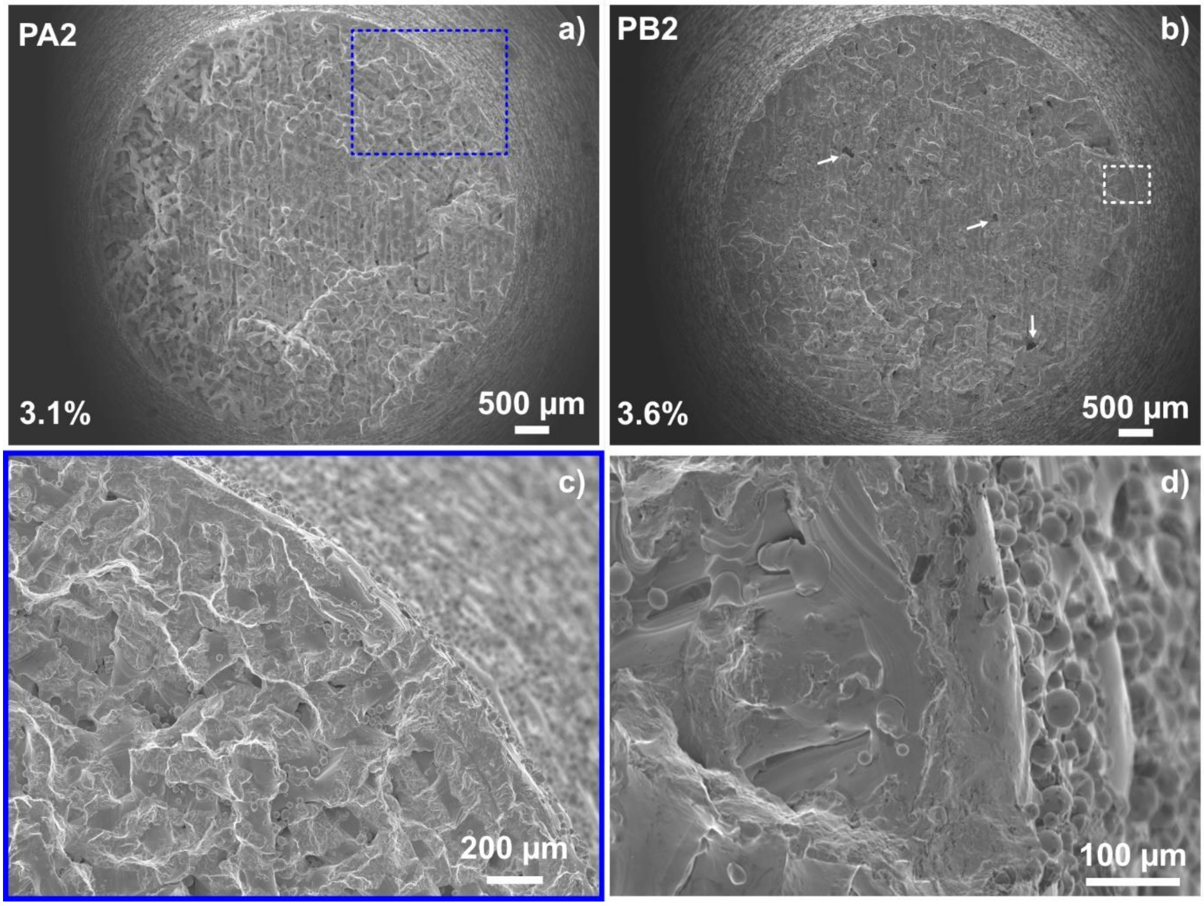

Figure 27: Scanning electron microscopy (SEM) images of fracture surfaces of (a, c) PA2 and (b, d) PB2 samples after fatigue testing. Higher magnification images of the regions highlighted by the dashed boxes in (a) and (b) are shown in (c) and (d), respectively, revealing potential crack initiation sites.

5.2 Productivity of low alloy steel

Paper III aimed to enhance the build speed of low alloy steels produced by PBF-LB, using prior parameter development [92] as a benchmark, given their relevance in cost-sensitive industries like automotive [111]. A primary finding was that the carbon content acted as a constraint on the achievable build rate for these steels. Attempts to increase build speed by elevating scan speed resulted in shallower melt pools and reduced in-situ tempering. This, coupled with high hardness and residual stresses, led to cold cracking, particularly in the higher carbon 4140 alloy. Consequently, the 4130 alloy, with its lower carbon content, exhibited higher attainable build rates.

In some 4140 specimens, surface-initiated cracks, oriented perpendicular to the build direction and extending inwards (Figure 28c), were observed. Their small size did not significantly affect sample density. Prior research at a 20 µm layer thickness linked similar cracking to cold cracking through microhardness and fractography analysis [84]. An evaluation of hardness and melt pool depths revealed that increased SED correlated with deeper melt pools and lower hardness (Fig. 28a-b). For SED values between 2.4 and 3.8 J/mm², the 4140-alloy showed slightly higher hardness (400 – 450 HV10) compared to the 4130 alloy (350 – 400 HV10), with cracked samples highlighted in red (Fig. 28b). Crack-free samples were generally obtained above 3.4 J/mm² for both layer thicknesses. This is likely due to the larger melt volume at higher SED, promoting more effective in-situ tempering [112]. Furthermore, the higher carbon content in 4140 is suggested to increase its hardenability and susceptibility to cracking compared to 4130 [84].

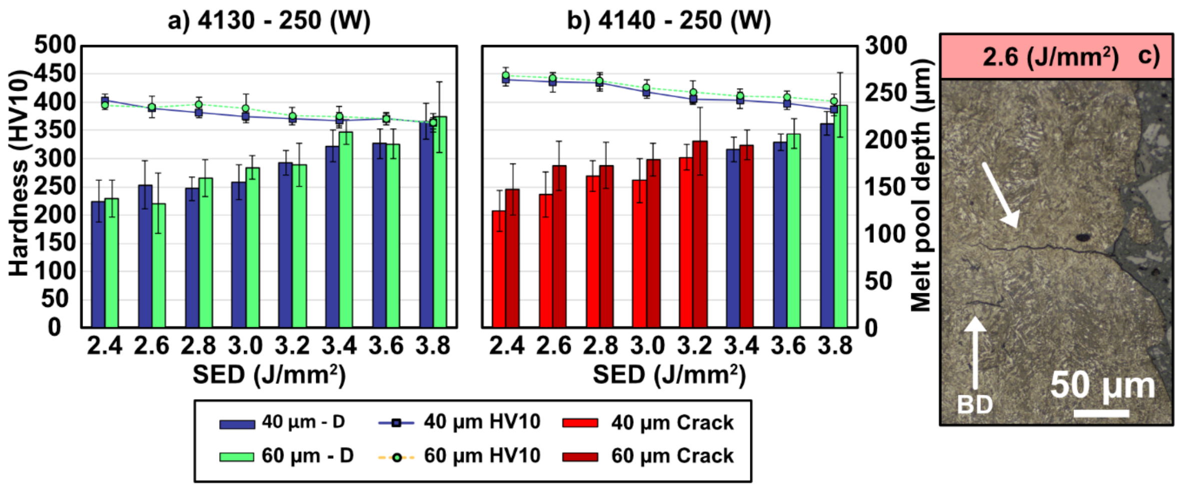

Figure 28: Hardness (HV10) and melt pool depth (µm) plotted against SED (J/mm²) for a) 4130 and b) 4140 steels, processed at a laser power of 250 W. Conditions representing specimens with cold cracks are highlighted in red.

5.3 Post-AM surface treatments and its impact on material properties

The following section summarizes the post-AM surface treatments of as-built surfaces using potential AM tailored surface material removal processes covered in **Paper IV** and **Paper V**.

5.3.1 Influence of Hirtisation® and chemical mechanical polishing on microstructure

The typical appearance of the as-built surface is presented in Fig. 29a with a surface roughness of Sa = ~20 µm. The Hirtisation® process reduced this roughness to approximately 7 µm Sa, primarily due to the removal of adhered powder (Fig. 29a). The topography after Hirtisation® (Fig. 29b) revealed melt pool boundaries, indicating preferential material removal locations. In contrast, chemical mechanical polishing (CMP) led to reductions as low as 0.7 µm Sa and yielded a different surface topography than Hirtisation®, where the surface was completely planarized by the removal of surface peaks with some valleys remaining (Fig. 29c). Also, note that microstructural features such as melt pools are not visible after CMP.

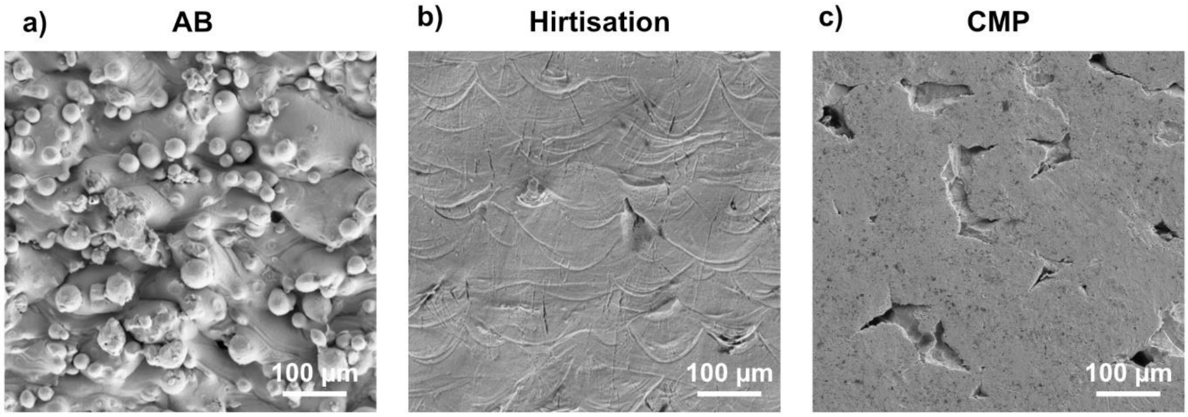

Figure 29: Surface topography of a) as-built surface b) after Hirtisation® and c) after CMP.

The mechanism of material removal for the Hirtisation® process, as observed at higher magnification in Figure 30, involved preferential attack near melt pool boundaries and, to some extent, along grain boundaries. This preferential removal is evident when comparing the as-built features (Fig. 23a) with the surface after Hirtisation® (Fig. 30b-c). While the exact cause of this was not investigated in detail, it is assumed to be related to local chemical variations at melt pool boundaries resulting from segregation during solidification [113]. Consequently, research into the effect of heat treatment on this phenomenon could provide further understanding of the underlying mechanism. Furthermore, two implications of this preferential removal were identified. First, the material removed near the melt pools left sharp notches (approximately 10 µm in depth). Further, anisotropic surface patterns were observed after Hirtisation® of microstructures induced by a 0° scan rotation, as seen in the differing cross-sections in Figure 30b and 30c. To mitigate this anisotropy and achieve more uniform material removal, **Paper IV** recommends the use of a 67° scan rotation, which yields more homogeneous as-built surfaces with less variation in microstructural features, resulting in more uniform material removal by the Hirtisation® process.

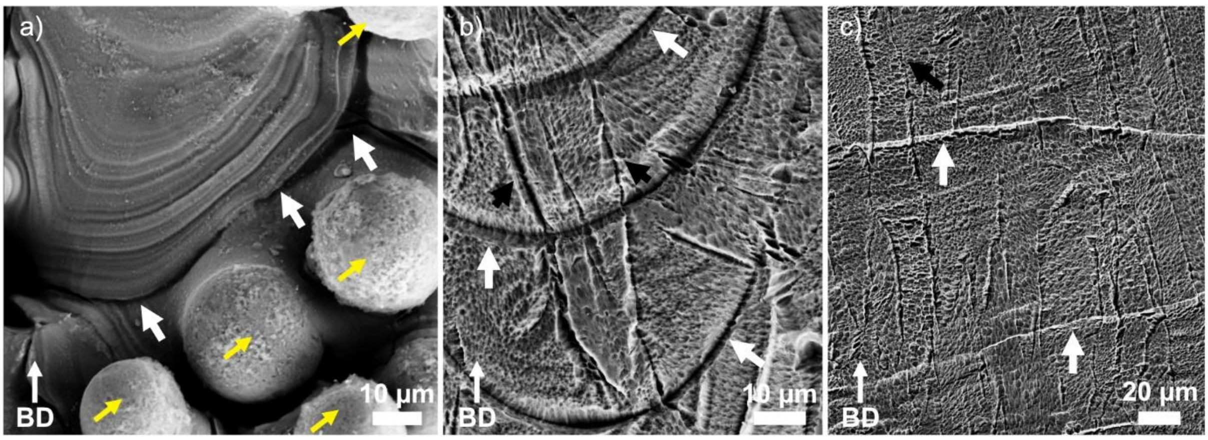

Figure 30: SEM images illustrating the preferential material removal during Hirtisation® near melt pool and grain boundaries. a) shows the as-built microstructure with melt pool boundaries (white arrows) and partially melted powder (yellow arrows). b) and c) reveal preferential attack along these boundaries during Hirtisation® on different cross-sections of a 0° scan rotation sample, leading to distinct surface patterns. Black arrows in b) and c) indicate grain boundaries also experiencing some attack.

In contrast to Hirtisation®, where microstructural features were preferentially attacked, CMP resulted in surface removal without any indication of preferential attacks near microstructural features, as supported by EBSD (Figure 31). The EBSD maps in Fig. 31a (as-built edge) and

Fig. 31b (CMP-treated edge) show no significant alteration of the microstructure or grain size near the edges, although a clear rounding of the edge is apparent. However, the EBSD analysis reveals the formation of a thin, deformed surface layer indicated by unindexed areas and confirmed by KAM maps showing increased misorientation. This suggested a mechanical effect at the near surface with surprisingly little impact on the surface microstructure.

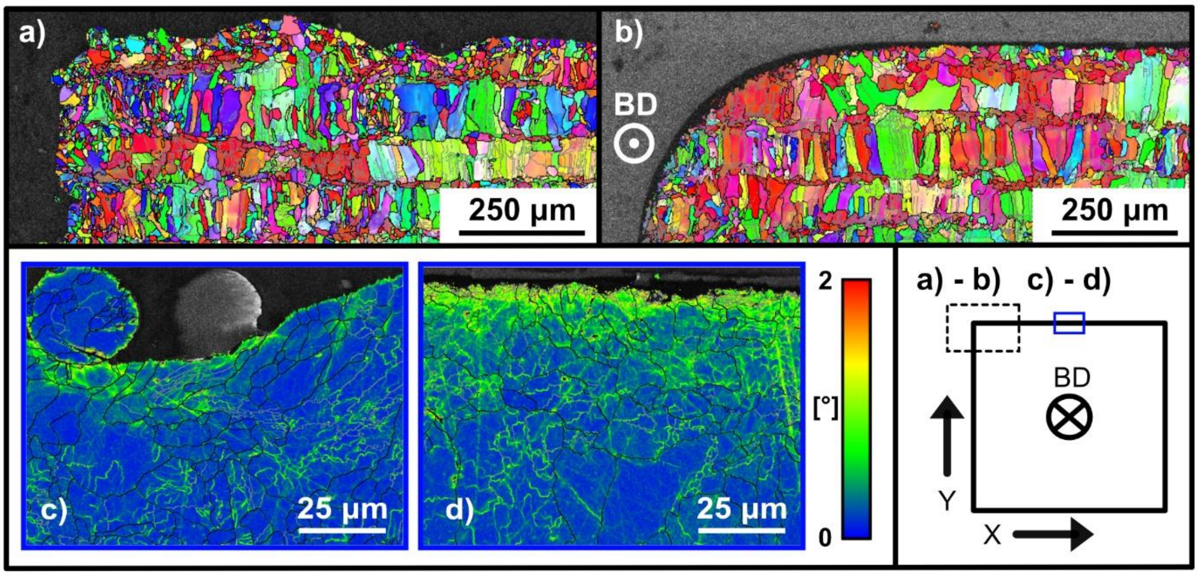

Figure 31: Microstructural analysis by EBSD near the edge of a 316L sample: (a) as built and (b) after CMP. The CMP-treated surface exhibits edge rounding and near-surface plastic deformation, as highlighted by the higher magnification KAM maps in (c) and (d). While CMP planarizes the surface, the EBSD maps show no significant alteration of the underlying grain structure, but the KAM maps reveal deformation close to the surface.

Based on the combined analysis of the surface topography and microstructure on PBF-LB 316L subjected to CMP or Hirtisation®, the main takeaways are presented in Figure 32. Both processes are affected by the anisotropic surface topography and microstructure generated by the 0° scan rotation, which can be seen by comparing the BD-Y and BD-X cross-sections. As stated earlier, the preferential attack of melt pools during Hirtisation® consequently yields different patterns. As for CMP, it is more a question of how much surface material should be removed. In this case, at least another 100 µm should have been removed to fully eliminate the valleys created between stacked melt pools of the BD-X cross-section, which was initially rougher with deeper valleys compared to the other cross-section.

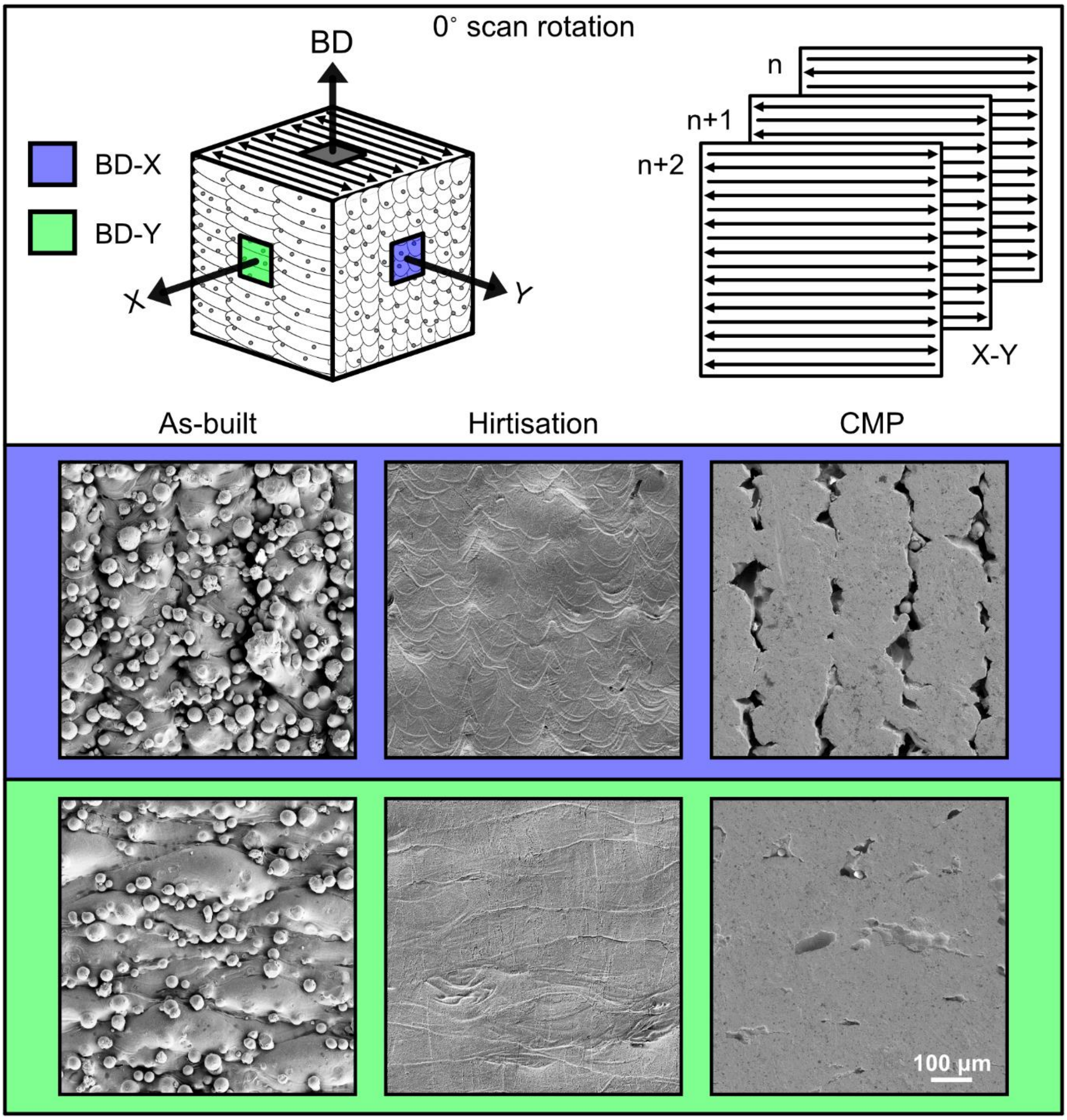

Figure 32: Visual representation of the impact of 0° scan rotation on surface topography and the effectiveness of Hirtisation® and CMP. Scanning electron micrographs compare the BD-X and BD-Y cross-sections in the as-built condition and after each surface treatment, illustrating how the initial anisotropic surface, created by the unidirectional scanning, influences the material removal and final surface morphology achieved by Hirtisation® and CMP.

5.3.2 Influence of Hirtisation® or CMP on subsurface residual stresses

As illustrated in Figure 33, Hirtisation® leads to an increase in tensile residual stress. Given that material removal via Hirtisation® is strictly an electrochemical process, the observed stress increase is likely attributed to stress redistribution compensating for the removal of approximately 150 µm of material. This finding presents a potential concern, as tensile stresses approaching the material yield limit were detected at a depth of 100 µm from the surface. In contrast, CMP induces compressive residual stress. This transition to a compressive stress state is likely associated with the mechanical action inherent to the CMP process and the resultant surface deformation, as discussed previously. Another observation was that the strain distribution of the samples processed by CMP was fully isotropic. The contrasting effects of these two post-processing methods on the residual stress state highlights the fundamental differences in their material removal mechanisms.

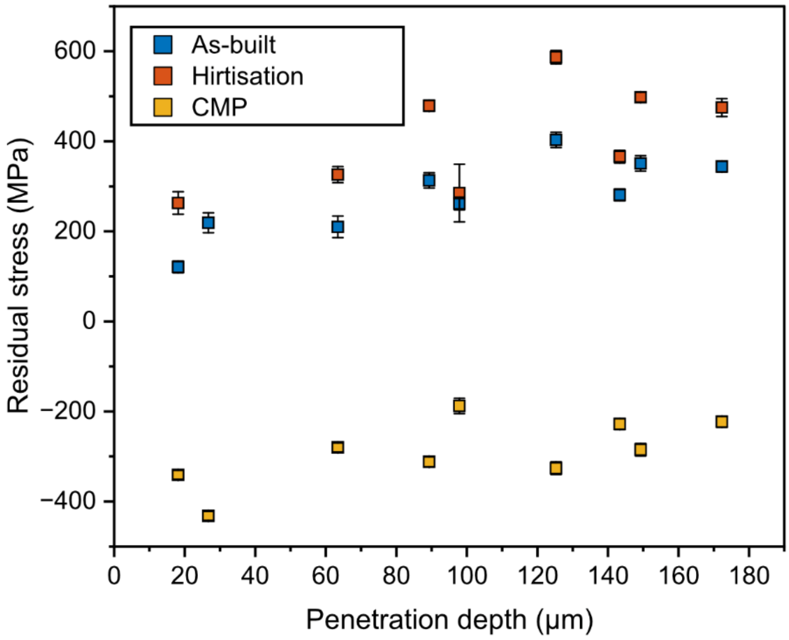

Figure 33: Influence of Hirtisation® and CMP post-processing on the residual stress profile of PBF-LB 316L as a function of depth from the surface. The as-built residual stress is shown for comparison. Data acquired via synchrotron X-ray diffraction (SXRD).

5.3.3 Fatigue life after surface treatments

In **Paper VI**, the fatigue behaviour of the reference material was evaluated following processing with both CMP and Hirtisation®. Subsequent testing demonstrated a significant improvement in endurance under cyclic loading for both surface treatments, resulting in a fatigue life approximately double that of the as-built condition (see Figure 34). Analysis of fracture surfaces indicated that crack initiation was frequently associated with pores that had become exposed at the surface in CMP-treated samples, while in Hirtisation® processed samples no obvious surface defects were found. These initiation sites in CMP samples likely correspond to the spherical pores previously identified by XCT (Fig. 25) within the contour/hatch overlap zone, situated roughly 100 µm below the surface. Consequently, it is possible that further gains in fatigue life could be achieved if these contour-induced pores were eliminated, particularly for CMP. In contrast, the absence of surface defects in Hirtisation® processed samples, where approximately 400 µm of material was removed, suggests that this process effectively eliminated these subsurface pores. Assuming comparable surface characteristics on the fatigue test specimens to those observed on the cubes used for microstructural analysis in **Paper IV**, crack initiation in Hirtisation® processed samples may have originated in the valleys formed between solidified melt tracks.

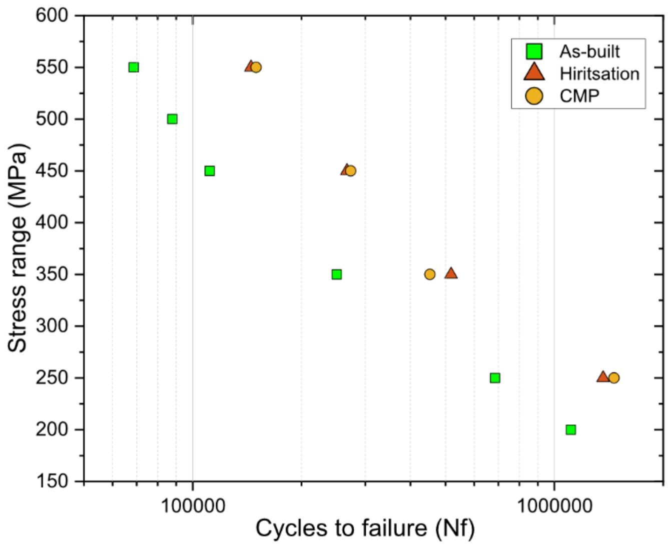

Figure 34: Fatigue life (Nf) as a function of stress range (MPa) for 316L samples in the as-built condition, after Hirtisation®, and after chemical mechanical processing.

6. Conclusions

This thesis investigated how increased build rates, enabled through systematic variation of the key PBF-LB process parameters, namely layer thickness, scan speed, and hatch distance, affect processability, porosity formation, surface characteristics, and fatigue performance in ferrous alloys, including 316L stainless and 4130 and 4140 low-alloy steels. Through a combination of empirical modelling, advanced pore characterization (2D and 3D), and surface treatment evaluation, the work provides new insights into the trade-offs between productivity and part quality. The conclusions are structured to directly address the three research questions that framed this research.

RQ1: How do high-productivity process parameters in PBF-LB influence the pore characteristics of ferrous alloys?

This research demonstrates that increasing build rates in PBF-LB through higher layer thickness, scan speed and hatch distance significantly affects pore formation in 316L stainless steel. The porosity response cannot be reliably predicted by VED alone, instead, the combined influence of layer thickness, scan speed, hatch distance, and laser power must be considered.

- In 316L, a ~120% increase in build rate produced pores aligned either parallel (by increased hatch distance) or perpendicular (by increased scan speed) to the build direction, affecting orientation and morphology. Elongated pores formed preferentially at high hatch distance and large layer thickness (80 µm), while smaller layer thicknesses allowed for more remelting and pore healing.
- The 3D XCT analysis revealed that traditional 2D imaging do not provide full information concerning pore morphology, particularly for large, sharp pores extending across multiple layers.
- In low-alloy steels (AISI 4130 and 4140), defect formation was found to be sensitive to surface energy density (SED). High SED mitigated LoF pores and cold cracking, enabling the production of crack-free, dense parts even at higher build rates (up to 250% increase for 4130).
- Cold cracking in 4140 was suppressed by increasing SED above 3.4 J/mm², promoting in-situ tempering and lowering hardness from ~450 to ~400 HV.

These findings provide process maps and guidelines for optimizing build rate without compromising part density, enabling tailored defect control in both stainless and low-alloy steels.

RQ2: How do as-built microstructure and surface roughness influence material removal during post-AM surface treatment?

Two advanced post-processing methods, Hirtisation® and Chemical Mechanical Polishing (CMP), were investigated for their ability to reduce the high surface roughness inherent to as-built PBF-LB components while preserving or enhancing microstructural integrity.

- Hirtisation® removed powder particles and preferentially attacked melt pool boundaries, leading to surface notches up to 10 µm deep. The process was sensitive to scan strategy where 67° scan rotation yielded more uniform surfaces than 0°, which produced anisotropic roughness.
- CMP achieved significant smoothing, reducing Sa roughness by up to 90% (as low as 0.7 µm). Surface peaks were fully removed, though valleys up to 90 µm remained in some regions, indicating that a material removal depth of ~110 µm was insufficient.

- Microstructural investigations showed that neither method significantly altered grain size, but CMP introduced shallow plastic deformation (1–5 µm) and rounded edges.
- Importantly, CMP induced compressive surface residual stress (up to −400 MPa) and promoted isotropic strain distribution, both of which are favorable for fatigue performance.

Thus, both techniques offer effective surface refinement. Hirtisation® is well-suited for complex internal geometries, while CMP provides mechanical enhancement through stress redistribution with minimal microstructural change.

RQ3: How do surface roughness and pore characteristics influence the fatigue strength of PBF-LB processed stainless steel?

Fatigue testing revealed that pore morphology and orientation were the dominant factors influencing high-cycle fatigue (HCF) performance in 316L, especially under as-built conditions.

- Fatigue life was significantly reduced at increased build rates, with samples produced via high scan speed (inter-layer porosity) exhibiting lower and more scattered fatigue performance due to randomly distributed, sharp LoF pores often connected to the surface and oriented perpendicular to loading.
- In contrast, parts produced with increased hatch distance (inter-hatch porosity) showed a more uniform pore distribution and lower scatter in fatigue life, despite similar porosity levels.
- Both CMP and Hirtisation® surface treatments improved fatigue life by approximately twofold. CMP exposed sub surface pores (spherical in shape) which acted as crack initiation points. As Hirtisation® removed ~400 µm of material, near-surface defects were fully removed.

These results highlight that fatigue strength is governed by the interaction of surface condition and subsurface porosity. For fatigue-sensitive applications, both the pore morphology and surface treatment strategy must be carefully engineered considering build rate optimization.

7. Future work

Based on the results and conclusions of this thesis, several areas for future research are recommended to advance the understanding and application of high-productivity PBF-LB of ferrous alloys.

Hot Isostatic Pressing (HIP) should be explored to compensate for the increased pore fractions associated with ultra-fast builds using large hatch distances and layer thicknesses. This approach could allow the process window to be intentionally widened, significantly boosting productivity. Additionally, the influence of different LoF pore morphologies, such as those observed in this work on the possibility to use HIP for their mitigation, needs investigation, particularly in terms of shape, orientation, and connectivity.

The choice of process gas during both printing and HIP (e.g., nitrogen vs. argon) should be studied for its potential to affect densification behavior, microstructure, and overall mechanical performance. This could be especially relevant for increasing the fatigue properties of 316L stainless steel.

Fatigue testing should be expanded to include a reference condition at 40 µm layer thickness, representing a common industrial standard. This would help contextualize the influence of increased build rates on high-cycle fatigue life. Furthermore, fatigue testing of samples built at different angles is recommended to investigate how pore orientation relative to the load direction affects crack initiation and propagation, particularly for LoF pores.

To isolate the effect of internal pore characteristics on fatigue strength, surface roughness should be removed by machining prior to testing. This would enable more precise evaluation of critical pore size and proximity to the surface. Similarly, while extensive tensile property data exists for 316L, it is important to test the specific parameter sets used in this thesis to understand how increased build rates and resulting pore types influence strength and ductility.

The mechanism behind the preferential material removal observed during Hirtisation®, particularly near melt pool boundaries, should be studied further. Effect of post-AM heat treatment on the surface response by Hirtisation® and CMP should be additionally studied.

Finally, determining the precise depth at which surface and subsurface features form in as-built parts is essential. This information is critical for guiding surface treatment providers on the appropriate amount of material removal required to eliminate defects and optimize surface integrity.

Acknowledgements

First and foremost, I extend my deepest gratitude to my supervisor, Prof. Eduard Hryha, for giving me the invaluable opportunity to pursue this PhD. His expertise, support, and extensive network within the field of additive manufacturing, particularly through CAM2, enabled important collaborations with both industry and academia. These connections played a key role in shaping my development as both a researcher and an engineer, and I will always value the friendships and partnerships formed along the way.

I am also sincerely thankful to Prof. Uta Klement for her invaluable guidance and unwavering support during the latter half of this journey. Her always-open door fostered constructive discussions and provided encouragement during some of the most challenging moments.

My thanks also go to Dr. Zhuoer Chen, who offered thoughtful guidance and consistent support during the early stages of my PhD. I greatly appreciated the productive discussions and his mentorship.

I would like to express my gratitude to Dr. Tatiana Mishurova for her collaboration and expert assistance with the synchrotron work at BAM, as well as to Dr. Jakob Schröder for his support during those experiments.

Beyond my supervisors and collaborators, I want to acknowledge the fantastic colleagues who made this experience so much more enjoyable over the years: William, Bala, Bharat, Alberto, Fardan, Anok, Gowtham, Dmitri, Sofia, Satya, Vishnu, Saith, Plinio and Antonio thank you for the inspiration and camaraderie. A special thank you to my officemates, Marcus and Erika, for making everyday work life lighter and more fun.

To my family, thank you for your unwavering support and encouragement. Your belief in me throughout these demanding years has meant everything.

Lastly, to my fiancé Tove, thank you from the bottom of my heart. Your steady support and understanding, especially during the intense final stages, has been truly beyond measure.

References

[1] D. Herzog, V. Seyda, E. Wycisk, C. Emmelmann, Additive manufacturing of metals, Acta Mater 117 (2016) 371–392. https://doi.org/10.1016/j.actamat.2016.07.019.

[2] T. DebRoy, H.L. Wei, J.S. Zuback, T. Mukherjee, J.W. Elmer, J.O. Milewski, A.M. Beese, A. Wilson-Heid, A. De, W. Zhang, Additive manufacturing of metallic components – Process, structure and properties, Prog Mater Sci 92 (2018) 112–224. https://doi.org/10.1016/j.pmatsci.2017.10.001.

[3] S. Sun, M. Brandt, M. Easton, Powder bed fusion processes, in: Laser Additive Manufacturing, Elsevier, 2017: pp. 55–77. https://doi.org/10.1016/B978-0-08-100433-3.00002-6.

[4] P. Paradise, D. Patil, N. Van Handel, S. Temes, A. Saxena, D. Bruce, A. Suder, S. Clonts, M. Shinde, C. Noe, D. Godfrey, R. Hota, D. Bhate, Improving Productivity in the Laser Powder Bed Fusion of Inconel 718 by Increasing Layer Thickness: Effects on Mechanical Behavior, J Mater Eng Perform 31 (2022) 6205–6220. https://doi.org/10.1007/s11665-022-06961-8.

[5] M. Leary, Economic feasibility and cost-benefit analysis, Fundamentals of Laser Powder Bed Fusion of Metals (2021) 597–620. https://doi.org/10.1016/B978-0-12-824090-8.00022-6.

[6] M. Taghian, M. Hossein, E. Lannunziata, G. Del, L. Iuliano, A. Saboori, Laser powder bed fusion of metallic components : Latest progress in productivity , quality , and cost perspectives, Journal of Materials Research and Technology 27 (2023) 6484–6500. https://doi.org/10.1016/j.jmrt.2023.11.049.

[7] W. Zhang, W. Hou, L. Deike, C.B. Arnold, Using a Dual-laser System to Create Periodic Coalescence in Laser Powder Bed Fusion, Acta Mater 201 (2020) 14–22. https://doi.org/10.1016/j.actamat.2020.09.071.

[8] C.S. Frandsen, M.M. Nielsen, A. Chaudhuri, J. Jayaram, K. Govindan, In search for classification and selection of spare parts suitable for additive manufacturing: a literature review, Int J Prod Res 58 (2020) 970–996. https://doi.org/10.1080/00207543.2019.1605226.

[9] M. Salmi, E. Pei, Additive manufacturing processes and materials for spare parts, Journal of Mechanical Science and Technology 37 (2023) 5979–5990. https://doi.org/10.1007/s12206-023-1034-0.

[10] H. Danninger, C. Gierl-Mayer Dr, Advanced powder metallurgy steel alloys, 2013. https://doi.org/10.1533/9780857098900.2.149.

[11] X. Liang, A. Hor, C. Robert, M. Salem, F. Lin, F. Morel, High cycle fatigue behavior of 316L steel fabricated by laser powder bed fusion: Effects of surface defect and loading mode, Int J Fatigue 160 (2022) 106843. https://doi.org/10.1016/j.ijfatigue.2022.106843.

[12] O. Andreau, E. Pessard, I. Koutiri, P. Peyre, N. Saintier, Influence of the position and size of various deterministic defects on the high cycle fatigue resistance of a 316L steel manufactured by laser powder bed fusion, Int J Fatigue 143 (2021) 105930. https://doi.org/10.1016/j.ijfatigue.2020.105930.

[13] B.D.L.F.W.K.H. Seifi Mohsen, ASM Handbook®, Volume 24A - Additive Manufacturing Design and Applications, ASM International, 2023. https://app.knovel.com/hotlink/toc/id:kpASMHVA52/asm-handbook-volume-24a/asm-handbook-volume-24a.

[14] A. 52900, Additive Manufacturing - General Principles - Terminology, 2021. https://www.iso.org/obp/ui/#iso:std:69669:en%0Ahttps://www.iso.org/standard/69669.html%0Ahttps://www.astm.org/Standards/ISOASTM52900.htm.

[15] R. Bär, P. Purtschert, Management Summary, Lean-Reporting (2014) 255–259. https://doi.org/10.1007/978-3-8348-2292-5_9.

[16] A. Vafadar, F. Guzzomi, A. Rassau, K. Hayward, Advances in metal additive manufacturing: A review of common processes, industrial applications, and current challenges, Applied Sciences (Switzerland) 11 (2021) 1–33. https://doi.org/10.3390/app11031213.

[17] N. Haghdadi, M. Laleh, M. Moyle, S. Primig, Additive manufacturing of steels: a review of achievements and challenges, J Mater Sci 56 (2021) 64–107. https://doi.org/10.1007/s10853-020-05109-0.

[18] S. Sanchez, P. Smith, Z. Xu, G. Gaspard, C.J. Hyde, W.W. Wits, I.A. Ashcroft, H. Chen, A.T. Clare, Powder Bed Fusion of nickel-based superalloys: A review, Int J Mach Tools Manuf 165 (2021). https://doi.org/10.1016/j.ijmachtools.2021.103729.

[19] P.A. Rometsch, Y. Zhu, X. Wu, A. Huang, Review of high-strength aluminium alloys for additive manufacturing by laser powder bed fusion, Mater Des 219 (2022) 110779. https://doi.org/10.1016/j.matdes.2022.110779.

[20] T.S. Tshephe, S.O. Akinwamide, E. Olevsky, P.A. Olubambi, Additive manufacturing of titanium-based alloys- A review of methods, properties, challenges, and prospects, Heliyon 8 (2022) e09041. https://doi.org/10.1016/j.heliyon.2022.e09041.

[21] C.A. Biffi, J. Fiocchi, S. Boldrini, A. Tuissi, CuCrZr Alloy Manufactured by LPBF Process: Correlation Between Microstructure, Mechanical and Thermal Properties, Lasers in Manufacturing and Materials Processing 11 (2024) 143–153. https://doi.org/10.1007/s40516-023-00240-7.

[22] C. Pauzon, E. Hryha, P. Forêt, L. Nyborg, Effect of argon and nitrogen atmospheres on the properties of stainless steel 316 L parts produced by laser-powder bed fusion, Mater Des 179 (2019). https://doi.org/10.1016/j.matdes.2019.107873.

[23] J.P. Oliveira, A.D. LaLonde, J. Ma, Processing parameters in laser powder bed fusion metal additive manufacturing, Mater Des 193 (2020) 1–12. https://doi.org/10.1016/j.matdes.2020.108762.

[24] Z. Dong, Y. Liu, W. Wen, J. Ge, J. Liang, Effect of hatch spacing on melt pool and as-built quality during selective laser melting of stainless steel: Modeling and experimental approaches, Materials 12 (2018). https://doi.org/10.3390/ma12010050.

[25] M. Tang, P.C. Pistorius, J.L. Beuth, Prediction of lack-of-fusion porosity for powder bed fusion, Addit Manuf 14 (2017) 39–48. https://doi.org/10.1016/j.addma.2016.12.001.

[26] I. Yadroitsev, A. Gusarov, I. Yadroitsava, I. Smurov, Single track formation in selective laser melting of metal powders, J Mater Process Technol 210 (2010) 1624–1631. https://doi.org/10.1016/j.jmatprotec.2010.05.010.

[27] A. Bobel, L.G. Hector, I. Chelladurai, A.K. Sachdev, T. Brown, W.A. Poling, R. Kubic, B. Gould, C. Zhao, N. Parab, A. Greco, T. Sun, In situ synchrotron X-ray imaging of 4140 steel laser powder bed fusion, Materialia (Oxf) 6 (2019) 100306. https://doi.org/10.1016/j.mtla.2019.100306.

[28] S.L. Campanelli, N. Contuzzi, P. Posa, A. Angelastro, Printability and microstructure of selective laser melting of WC/Co/Cr powder, Materials 12 (2019). https://doi.org/10.3390/ma12152397.

[29] A. Gatto, M.L. Gatto, R. Groppo, D. Munteanu, P. Mengucci, Influence of laser powder bed fusion process parameters on the properties of CuZn42 components: case study of the laser surface energy density, Progress in Additive Manufacturing 8 (2023) 843–855. https://doi.org/10.1007/s40964-022-00361-z.

[30] U. Scipioni Bertoli, A.J. Wolfer, M.J. Matthews, J.P.R. Delplanque, J.M. Schoenung, On the limitations of Volumetric Energy Density as a design parameter for Selective Laser Melting, Mater Des 113 (2017) 331–340. https://doi.org/10.1016/j.matdes.2016.10.037.

[31] O. Diegel, A. Nordin, D. Motte, A Practical Guide to Design for Additive Manufacturing, 2019.

[32] A. Ezura, S. Abe, T. Furumoto, T. Sasaki, J. Sakamoto, Study on Laser Scan Strategy for Correcting Anisotropic Residual Stress Distribution and Reducing Warpage in Structures Fabricated by PBF-LB/M, International Journal of Automation Technology 17 (2023) 369–377. https://doi.org/10.20965/ijat.2023.p0369.

[33] A. Leicht, C.H. Yu, V. Luzin, U. Klement, E. Hryha, Effect of scan rotation on the microstructure development and mechanical properties of 316L parts produced by laser powder bed fusion, Mater Charact 163 (2020) 110309. https://doi.org/10.1016/j.matchar.2020.110309.

[34] R. Gunnerek, G. Soundarapandiyan, M. Christoph, E. Hryha, U. Klement, Transactions of the IMF The International Journal of Surface Engineering and Coatings Influence of microstructure and surface topography on material removal by the Hirtisation ® process, Transactions of the IMF 0 (2024) 1–8. https://doi.org/10.1080/00202967.2024.2411903.

[35] L. Guo, H. Wang, H. Liu, Y. Huang, Q. Wei, C.L.A. Leung, Y. Wu, H. Wang, Understanding keyhole induced-porosities in laser powder bed fusion of aluminum and elimination strategy, Int J Mach Tools Manuf 184 (2023). https://doi.org/10.1016/j.ijmachtools.2022.103977.

[36] W.H. Kan, L.N.S. Chiu, C.V.S. Lim, Y. Zhu, Y. Tian, D. Jiang, A. Huang, A critical review on the effects of process-induced porosity on the mechanical properties of alloys fabricated by laser powder bed fusion, J Mater Sci 57 (2022) 9818–9865. https://doi.org/10.1007/s10853-022-06990-7.

[37] C. Du, Y. Zhao, J. Jiang, Q. Wang, H. Wang, N. Li, J. Sun, Pore defects in Laser Powder Bed Fusion: Formation mechanism, control method, and perspectives, J Alloys Compd 944 (2023) 169215. https://doi.org/10.1016/j.jallcom.2023.169215.

[38] A. Sola, A. Nouri, Microstructural porosity in additive manufacturing: The formation and detection of pores in metal parts fabricated by powder bed fusion, J Adv Manuf Process 1 (2019) 1–21. https://doi.org/10.1002/amp2.10021.

[39] T. Montalbano, B.N. Briggs, J.L. Waterman, S. Nimer, C. Peitsch, J. Sopcisak, D. Trigg, S. Storck, Uncovering the coupled impact of defect morphology and microstructure on the tensile behavior of Ti-6Al-4V fabricated via laser powder bed fusion, J Mater Process Technol 294 (2021) 117113. https://doi.org/10.1016/j.jmatprotec.2021.117113.

[40] N. Yodoshi, T. Endo, N. Masahashi, Evaluation of porosity in gas-atomized powder by synchrotron X-ray CT and investigation of the effect of gas species, Mater Trans 62 (2021) 1549–1555. https://doi.org/10.2320/matertrans.MT-Y2021001.

[41] Z. Li, H. Li, J. Yin, Y. Li, Z. Nie, X. Li, D. You, K. Guan, W. Duan, L. Cao, D. Wang, L. Ke, Y. Liu, P. Zhao, L. Wang, K. Zhu, Z. Zhang, L. Gao, L. Hao, A Review of Spatter in Laser Powder Bed Fusion Additive Manufacturing: In Situ Detection, Generation, Effects, and Countermeasures, Micromachines (Basel) 13 (2022). https://doi.org/10.3390/mi13081366.

[42] Z.A. Young, Q. Guo, N.D. Parab, C. Zhao, M. Qu, L.I. Escano, K. Fezzaa, W. Everhart, T. Sun, L. Chen, Types of spatter and their features and formation mechanisms in laser powder bed fusion additive manufacturing process, Addit Manuf 36 (2020) 101438. https://doi.org/10.1016/j.addma.2020.101438.

[43] J.C. Snyder, K.A. Thole, Understanding Laser Powder Bed Fusion Surface Roughness, J Manuf Sci Eng 142 (2020). https://doi.org/10.1115/1.4046504.

[44] R. Wrobel, L. Del Guidice, P. Scheel, N. Abando, X. Maeder, M. Vassiliou, E. Hosseini, R. Spolenak, C. Leinenbach, Influence of wall thickness on microstructure and mechanical properties of thin-walled 316L stainless steel produced by laser powder bed fusion, Mater Des 238 (2024) 112652. https://doi.org/10.1016/j.matdes.2024.112652.

[45] C.H. Yu, R.L. Peng, V. Luzin, M. Sprengel, M. Calmunger, J.E. Lundgren, H. Brodin, A. Kromm, J. Moverare, Thin-wall effects and anisotropic deformation mechanisms of an additively manufactured Ni-based superalloy, Addit Manuf 36 (2020). https://doi.org/10.1016/j.addma.2020.101672.

[46] J.-Y. Lee, A.P. Nagalingam, S.H. Yeo, A review on the state-of-the-art of surface finishing processes and related ISO/ASTM standards for metal additive manufactured components, Virtual Phys Prototyp 16 (2021) 68–96. https://doi.org/10.1080/17452759.2020.1830346.

[47] J. Gockel, L. Sheridan, B. Koerper, B. Whip, The influence of additive manufacturing processing parameters on surface roughness and fatigue life, Int J Fatigue 124 (2019) 380–388. https://doi.org/10.1016/j.ijfatigue.2019.03.025.

[48] K. Artzt, T. Mishurova, P.P. Bauer, J. Gussone, P. Barriobero-Vila, S. Evsevleev, G. Bruno, G. Requena, J. Haubrich, Pandora's box-influence of contour parameters on roughness and subsurface residual stresses in laser powder bed fusion of Ti-6Al-4V, Materials 13 (2020) 1–24. https://doi.org/10.3390/ma13153348.

[49] T. Reiber, J. Rüdesheim, M. Weigold, E. Abele, J. Musekamp, M. Oechsner, Influence of contour scans on surface roughness and pore formation using Scalmalloy®

manufactured by laser powder bed fusion (PBF-LB), Materwiss Werksttech 52 (2021) 468–481. https://doi.org/10.1002/mawe.202000287.

[50] J. Schröder, A. Evans, T. Mishurova, A. Ulbricht, M. Sprengel, I. Serrano-Munoz, T. Fritsch, A. Kromm, T. Kannengießer, G. Bruno, Diffraction-based residual stress characterization in laser additive manufacturing of metals, 2021. https://doi.org/10.3390/met11111830.

[51] P.A. Hooper, Melt pool temperature and cooling rates in laser powder bed fusion, Addit Manuf 22 (2018) 548–559. https://doi.org/10.1016/j.addma.2018.05.032.

[52] T. Mishurova, K. Artzt, B. Rehmer, J. Haubrich, L. Ávila, F. Schoenstein, I. Serrano-Munoz, G. Requena, G. Bruno, Separation of the impact of residual stress and microstructure on the fatigue performance of LPBF Ti-6Al-4V at elevated temperature, Int J Fatigue 148 (2021). https://doi.org/10.1016/j.ijfatigue.2021.106239.

[53] M. Berghaus, S. Florian, K. Solanki, C. Zinn, H. Wang, B. Butz, H. Apmann, A. von Hehl, Effect of high laser scanning speed on microstructure and mechanical properties of additively manufactured 316L, Progress in Additive Manufacturing 10 (2024) 1119–1132. https://doi.org/10.1007/s40964-024-00693-y.

[54] A. Leicht, M. Rashidi, U. Klement, E. Hryha, Effect of process parameters on the microstructure, tensile strength and productivity of 316L parts produced by laser powder bed fusion, Mater Charact 159 (2020) 110016. https://doi.org/10.1016/j.matchar.2019.110016.

[55] D. Herzog, K. Bartsch, B. Bossen, Productivity optimization of laser powder bed fusion by hot isostatic pressing, Addit Manuf 36 (2020) 101494. https://doi.org/10.1016/j.addma.2020.101494.

[56] M. Kasprowicz, A. Pawlak, P. Jurkowski, T. Kurzynowski, Ways to increase the productivity of L-PBF processes, Archives of Civil and Mechanical Engineering 23 (2023). https://doi.org/10.1007/s43452-023-00750-3.

[57] C. Schwerz, F. Schulz, E. Natesan, L. Nyborg, Increasing productivity of laser powder bed fusion manufactured Hastelloy X through modification of process parameters, J Manuf Process 78 (2022) 231–241. https://doi.org/10.1016/j.jmapro.2022.04.013.

[58] S. McConnell, Y. Gaber, K.I. Kourousis, D. Tanner, Increasing productivity for Laser Powder Bed Fusion of Ti-6Al-4V parts through increased layer heights, Progress in Additive Manufacturing (2024). https://doi.org/10.1007/s40964-025-01079-4.

[59] L. Bauch, F. Winklbauer, T. Stittgen, A. Collet, J.H. Schleifenbaum, Estimation of Printing Time for Laser-Based Powder Bed Fusion of Metals, ASTM Special Technical Publication STP 1644 (2022) 14–28. https://doi.org/10.1520/STP164420210127.

[60] F. Huber, M. Rasch, M. Schmidt, Laser powder bed fusion (Pbf-lb/m) process strategies for in-situ alloy formation with high-melting elements, Metals (Basel) 11 (2021) 1–15. https://doi.org/10.3390/met11020336.

[61] E.B. Glaubitz, J.C. Fox, O.L. Kafka, J. Gockel, Contour parameters, melt pool behavior, and surface roughness relationships across laser powder bed fusion platforms and metallic alloys, International Journal of Advanced Manufacturing Technology (2025) 4419–4437. https://doi.org/10.1007/s00170-025-15066-0.

[62] V. Mercurio, F. Calignano, L. Iuliano, Sustainable production of AlSi10Mg parts by laser powder bed fusion process, International Journal of Advanced Manufacturing Technology 125 (2023) 3117–3133. https://doi.org/10.1007/s00170-023-11004-0.

[63] H. Choo, L.P. White, X. Xiao, C.C. Sluss, D. Morin, E. Garlea, Deformation and fracture behavior of a laser powder bed fusion processed stainless steel: In situ synchrotron x-ray computed microtomography study, Addit Manuf 40 (2021) 101914. https://doi.org/10.1016/j.addma.2021.101914.

[64] H. Gong, K. Rafi, H. Gu, G.D. Janaki Ram, T. Starr, B. Stucker, Influence of defects on mechanical properties of Ti-6Al-4V components produced by selective laser melting and electron beam melting, Mater Des 86 (2015) 545–554. https://doi.org/10.1016/j.matdes.2015.07.147.

[65] W.Y. Kim, E.Y. Yoon, J.H. Kim, S. Kim, Surface Characteristics of Ti–6Al–4V Alloy Based on the Process Parameter and Abrasive Process in the Laser Powder Bed Fusion, Metals and Materials International 29 (2023) 2345–2357. https://doi.org/10.1007/s12540-022-01378-3.

[66] H. Fayazfar, J. Sharifi, M.K. Keshavarz, M. Ansari, An overview of surface roughness enhancement of additively manufactured metal parts: a path towards removing the post-print bottleneck for complex geometries, Springer London, 2023. https://doi.org/10.1007/s00170-023-10814-6.

[67] R. Shrestha, J. Simsiriwong, N. Shamsaei, Fatigue behavior of additive manufactured 316L stainless steel parts: Effects of layer orientation and surface roughness, Addit Manuf 28 (2019) 23–38. https://doi.org/10.1016/j.addma.2019.04.011.

[68] S. Lee, J. Pegues, N. Shamsaei, Fatigue behavior of additive manufactured 304L stainless steel including surface roughness effects, in: Solid Freeform Fabrication 2019: Proceedings of the 30th Annual International Solid Freeform Fabrication Symposium - An Additive Manufacturing Conference, SFF 2019, 2019: pp. 376–387.

[69] J.C. Snyder, C.K. Stimpson, K.A. Thole, D.J. Mongillo, Build Direction Effects on Microchannel Tolerance and Surface Roughness, Journal of Mechanical Design 137 (2015). https://doi.org/10.1115/1.4031071.

[70] H. Zeidler, F. Böttger-Hiller, S. Krinke, P. Parenti, M. Annoni, Surface finish of additively manufactured parts using plasma electrolytic polishing, in: European Society for Precision Engineering and Nanotechnology, Conference Proceedings - 19th International Conference and Exhibition, EUSPEN 2019, 2019: pp. 228–229.

[71] A.W. Hashmi, H.S. Mali, A. Meena, A.P.V. Puerta, M.E. Kunkel, Surface characteristics improvement methods for metal additively manufactured parts: a review, Advances in Materials and Processing Technologies 8 (2022) 4524–4563. https://doi.org/10.1080/2374068X.2022.2077535.

[72] V. Sandell, J. Nilsson, T. Hansson, P. Åkerfeldt, M.L. Antti, Effect of chemical post-processing on surfaces and sub-surface defects in electron beam melted Ti-6Al-4V, Mater Charact 193 (2022) 8–14. https://doi.org/10.1016/j.matchar.2022.112281.

[73] G. Demeneghi, P. Gradl, A. Diaz, K. Hazeli, Effect of Surface Finish and Temperature on Low Cycle Fatigue Behavior of GRCop-42, Fatigue Fract Eng Mater Struct (2024) 840–856. https://doi.org/10.1111/ffe.14526.

[74] Z. Que, T. Riipinen, P. Ferreirós, S. Goel, K. Sipilä, T. Saario, T. Ikäläinen, A. Toivonen, A. Revuelta, Effects of surface finishes, heat treatments and printing orientations on stress corrosion cracking behavior of laser powder bed fusion 316L stainless steel in high-temperature water, Corros Sci 233 (2024). https://doi.org/10.1016/j.corsci.2024.112118.

[75] ISF Process for Metal Superfinishing- REM Surface Engineering, (n.d.). https://www.remchem.com/technology/processes/isf-process/ (accessed March 20, 2025).

[76] S. Prochaska, O. Hildreth, Effect of chemically accelerated vibratory finishing on the corrosion behavior of Laser Powder Bed Fusion 316L stainless steel, J Mater Process Technol 305 (2022) 117596. https://doi.org/10.1016/j.jmatprotec.2022.117596.

[77] T. Risposi, L. Rusnati, L. Patriarca, A. Hardaker, D. Luczyniec, S. Beretta, Fatigue of Ti6Al4V manufactured by PBF-LB: A comparison of failure mechanisms between net-shape and electro-chemically milled surface conditions, Eng Fail Anal 172 (2025) 109403. https://doi.org/10.1016/j.engfailanal.2025.109403.

[78] ASM Handbook, Heat Treating of steel, Metals Handbook 4 (1991) 14–367.

[79] K. Li, T. Yang, N. Gong, J. Wu, X. Wu, D.Z. Zhang, L.E. Murr, Additive manufacturing of ultra-high strength steels: A review, J Alloys Compd 965 (2023) 171390. https://doi.org/10.1016/j.jallcom.2023.171390.

[80] W. Hearn, E. Hryha, Effect of Carbon Content on the Processability of Fe-C Alloys Produced by Laser Based Powder Bed Fusion, Front Mater 8 (2022) 1–10. https://doi.org/10.3389/fmats.2021.800021.

[81] W. Hearn, P. Harlin, E. Hryha, Development of powder bed fusion–laser beam process for AISI 4140, 4340 and 8620 low-alloy steel, Powder Metallurgy 66 (2023) 94–106. https://doi.org/10.1080/00325899.2022.2134083.

[82] E.H. Sabuz, I. Shabib, Microstructure, Hardness, and Tensile Properties of Additively Manufactured Low-Alloy Steel: A Review, 2025. https://doi.org/10.1002/srin.202400421.

[83] X. Li, Y.H. Tan, H.J. Willy, P. Wang, W. Lu, M. Cagirici, C.Y.A. Ong, T.S. Herng, J. Wei, J. Ding, Heterogeneously tempered martensitic high strength steel by selective laser melting and its micro-lattice: Processing, microstructure, superior performance and mechanisms, Mater Des 178 (2019) 107881. https://doi.org/10.1016/j.matdes.2019.107881.

[84] W. Hearn, R. Steinlechner, E. Hryha, Laser-based powder bed fusion of non-weldable low-alloy steels, Powder Metallurgy 0 (2021) 1–12. https://doi.org/10.1080/00325899.2021.1959695.

[85] T. Fedina, J. Sundqvist, A.F.H. Kaplan, Spattering and oxidation phenomena during recycling of low alloy steel powder in Laser Powder Bed Fusion, Mater Today Commun 27 (2021) 102241. https://doi.org/10.1016/j.mtcomm.2021.102241.

[86] M. Abdelwahed, S. Bengtsson, R. Casati, A. Larsson, S. Petrella, M. Vedani, Effect of water atomization on properties of type 4130 steel processed by L-PBF, Mater Des 210 (2021) 110085. https://doi.org/10.1016/j.matdes.2021.110085.

[87] M. Abdelwahed, R. Casati, A. Larsson, S. Petrella, S. Bengtsson, M. Vedani, On the Recycling of Water Atomized Powder and the Effects on Properties of L-PBF Processed 4130 Low-Alloy Steel, Materials 15 (2022). https://doi.org/10.3390/ma15010336.

[88] W. Wang, S. Kelly, A Metallurgical Evaluation of the Powder-Bed Laser Additive Manufactured 4140 Steel Material, Jom 68 (2016) 869–875. https://doi.org/10.1007/s11837-015-1804-y.

[89] J. Damon, R. Koch, D. Kaiser, G. Graf, S. Dietrich, V. Schulze, Process development and impact of intrinsic heat treatment on the mechanical performance of selective laser melted AISI 4140, Addit Manuf 28 (2019) 275–284. https://doi.org/10.1016/j.addma.2019.05.012.

[90] E. Jelis, M.R. Hespos, N.M. Ravindra, Process Evaluation of AISI 4340 Steel Manufactured by Laser Powder Bed Fusion, J Mater Eng Perform 27 (2018) 63–71. https://doi.org/10.1007/s11665-017-2989-8.

[91] E. Jelis, M. Hespos, S.L. Groeschler, R. Carpenter, L-PBF of 4340 Low Alloy Steel: Influence of Feedstock Powder, Layer Thickness, and Machine Maintenance, J Mater Eng Perform 28 (2019) 693–700. https://doi.org/10.1007/s11665-018-3739-2.

[92] W. Hearn, Development of Structural Steels for Powder Bed Fusion – Laser Beam, 2023. https://research.chalmers.se/publication/534092%0Ahttps://research.chalmers.se/publication/534092/file/534092_Fulltext.pdf.

[93] J.R. Davis, 26.9 Austenitic Stainless Steels, ASM Specialty Handbook - Stainless Steels (1994). https://app.knovel.com/hotlink/khtml/id:kt00URSD21/asm-specialty-handbook/asm-specia-austenitic-2 (accessed May 13, 2025).

[94] H. Fayazfar, M. Salarian, A. Rogalsky, D. Sarker, P. Russo, V. Paserin, E. Toyserkani, A critical review of powder-based additive manufacturing of ferrous alloys: Process parameters, microstructure and mechanical properties, Mater Des 144 (2018) 98–128. https://doi.org/10.1016/j.matdes.2018.02.018.

[95] S. Wang, Y. Liu, W. Shi, B. Qi, J. Yang, F. Zhang, D. Han, Y. Ma, Research on high layer thickness fabricated of 316L by selective laser melting, Materials 10 (2017). https://doi.org/10.3390/ma10091055.

[96] A. Leicht, M. Rashidi, U. Klement, E. Hryha, Effect of process parameters on the microstructure, tensile strength and productivity of 316L parts produced by laser powder bed fusion, Mater Charact 159 (2020). https://doi.org/10.1016/j.matchar.2019.110016.

[97] O. Andreau, E. Pessard, I. Koutiri, J.D. Penot, C. Dupuy, N. Saintier, P. Peyre, A competition between the contour and hatching zones on the high cycle fatigue behaviour of a 316L stainless steel: Analyzed using X-ray computed tomography, Materials Science and Engineering: A 757 (2019) 146–159. https://doi.org/10.1016/j.msea.2019.04.101.

[98] D. Sheet, EOS Stainless-, n.d. https://www.eos.info/05-datasheet-images/Assets_MDS_Metal/EOS_StainlessSteel_316l/material_datasheet_eos_stainlessteel_316l_en_web.pdf.

[99] A. Leicht, M. Fischer, U. Klement, L. Nyborg, E. Hryha, Increasing the Productivity of Laser Powder Bed Fusion for Stainless Steel 316L through Increased Layer Thickness, J Mater Eng Perform 30 (2021) 575–584. https://doi.org/10.1007/s11665-020-05334-3.

[100] C.A. Schneider, W.S. Rasband, K.W. Eliceiri, NIH Image to ImageJ: 25 years of image analysis, Nat Methods 9 (2012) 671–675. https://doi.org/10.1038/nmeth.2089.

[101] R. Gunnerek, Z. Chen, E. Hryha, Impact of high-productivity process parameters in powder bed fusion – laser beam on microstructure of stainless steel 316L, European Journal of Materials 3 (2023). https://doi.org/10.1080/26889277.2023.2292987.

[102] A.J. Schwartz, M. Kumar, B.L. Adams, D.P. Field, Electron backscatter diffraction in materials science, 2009. https://doi.org/10.1007/978-0-387-88136-2.

[103] H. Markötter, M. Sintschuk, R. Britzke, S. Dayani, G. Bruno, D. Bhattacharyya, Upgraded imaging capabilities at the BAMline (BESSY II), J Synchrotron Radiat 29 (2022) 1292–1298. https://doi.org/10.1107/S1600577522007342.

[104] R. Farla, S. Bhat, S. Sonntag, A. Chanyshev, S. Ma, T. Ishii, Z. Liu, A. Néri, N. Nishiyama, G.A. Faria, T. Wroblewski, H. Schulte-Schrepping, W. Drube, O. Seeck, T. Katsura, Extreme conditions research using the large-volume press at the P61B endstation, PETRA III, J Synchrotron Radiat 29 (2022) 409–423. https://doi.org/10.1107/S1600577522001047.

[105] F. Cabanettes, A. Joubert, G. Chardon, V. Dumas, J. Rech, C. Grosjean, Z. Dimkovski, Topography of as built surfaces generated in metal additive manufacturing: A multi scale analysis from form to roughness, Precis Eng 52 (2018) 249–265. https://doi.org/10.1016/j.precisioneng.2018.01.002.

[106] SIS (Swedish Standards Institute), Svensk Standard, Ss 812310:2014 (2018) 24. www.sis.se.

[107] A. Ceramics, A. Ceramics, K. Hard-, A.B. Hardness, V. Hardness, S. Hardness, K. Hardness, L. Hardness, C. Techniques, P. Control, C. Laboratories, Standard Test Method for Microindentation Hardness of Materials BT - Standard Test Method for Microindentation Hardness of Materials, (17AD) 1–40. https://doi.org/10.1520/E0384-17.

[108] R. Gunnerek, Z. Chen, E. Hryha, Impact of high-productivity process parameters in powder bed fusion–laser beam on microstructure of stainless steel 316L, European Journal of Materials 3 (2023). https://doi.org/10.1080/26889277.2023.2292987.

[109] T. Ronneberg, C.M. Davies, P.A. Hooper, Revealing relationships between porosity, microstructure and mechanical properties of laser powder bed fusion 316L stainless steel through heat treatment, Mater Des 189 (2020) 108481. https://doi.org/10.1016/j.matdes.2020.108481.

[110] R. Gunnerek, T. Mishurova, G. Bruno, E. Hryha, Correlation between High Build Speed Process Parameters and Pore Characteristics of 316L Stainless Steel Manufactured by Powder Bed Fusion – Laser Beam, Journal of the Japan Society of Powder and Powder Metallurgy 72 (2025) 15B-T6-21. https://doi.org/10.2497/jjspm.15B-T6-21.

[111] J. Damon, R. Koch, D. Kaiser, G. Graf, S. Dietrich, V. Schulze, Process development and impact of intrinsic heat treatment on the mechanical performance of selective laser

melted AISI 4140, Addit Manuf 28 (2019) 275–284. https://doi.org/10.1016/j.addma.2019.05.012.

[112] W. Hearn, K. Lindgren, J. Persson, E. Hryha, In situ tempering of martensite during laser powder bed fusion of Fe-0.45C steel, Materialia (Oxf) 23 (2022). https://doi.org/10.1016/j.mtla.2022.101459.

[113] M.H. Ghoncheh, A. Shahriari, N. Birbilis, M. Mohammadi, Process-microstructure-corrosion of additively manufactured steels: a review, Critical Reviews in Solid State and Materials Sciences 0 (2023) 1–111. https://doi.org/10.1080/10408436.2023.2255616.

PAPER I

Impact of high-productivity process parameters in powder bed fusion – laser beam on microstructure of stainless steel 316L

Rasmus Gunnerek, Zhouer Chen and Eduard Hryha

European Journal of Materials, 2023

DOI: 10.1080/26889277.2023.2292987

PAPER II

Correlation between high build speed process parameters and pore characteristics of 316L stainless steel manufactured by powder bed fusion laser beam

Rasmus Gunnerek, Tatiana Mishurova, Giovanni Bruno and Eduard Hryha

Journal of the Japan Society of Powder and Powder Metallurgy, 2025

DOI:10.2497/jjspm.15B-T6-21

PAPER III

Improving productivity of low-alloy steels produced by powder bed fusion – laser beam

Rasmus Gunnerek, William Hearn and Eduard Hryha

Manuscript

PAPER IV

Influence of microstructure and surface topography on material removal by the Hirtisation® process

Rasmus Gunnerek, Gowtham Soundarapandiyan, Michael Christoph Doppler, Eduard Hryha and Uta Klement

Transactions of the IMF, 2024

DOI: 10.1080/00202967.2024.2411903

PAPER V

Chemical mechanical polishing of powder bed fusion – laser beam processed 316L stainless steel

Rasmus Gunnerek, Gowtham Soundarapandiyan, Tatiana Misuhrova, Jakob Schröder, Uta Klement and Eduard Hryha

Manuscript

PAPER VI

Influence of build rate and post-AM surface treatments on fatigue life of powder bed fusion – laser beam 316L stainless steel

Rasmus Gunnerek, Subhani Buddhika Kumarasinghe, Tatiana Misuhrova, Johan Moverare, Uta Klement and Eduard Hryha

Manuscript